View metadata, citation and similar papers at core.ac.uk
brought to you by CORE
provided by Servicio de Difusión de la Creación Intelectual

Mon. Not. R. Astron. Soc. **346,** 704–718 (2003)

XMM–Newton X-ray observations of the Carina nebula

J. F. Albacete Colombo,[1]★ M. Méndez[2] and N. I. Morrell[1]†‡§
[1]*Facultad de Ciencias Astronómicas y Geofísicas, Universidad Nacional de La Plata Paseo del Bosque S/N, 1900 La Plata, Argentina*
[2]*SRON, National Institute for Space Research, Sorbonnelaan 2, 3584 CA Utrecht, the Netherlands*

Accepted 2003 August 27. Received 2003 May 28; in original form 2002 December 3

ABSTRACT

We use new *XMM–Newton* observations to perform a detailed X-ray analysis of the Carina nebula region in the 0.3–12 keV energy range. Our source detection yields 80 discrete X-ray sources, from which about 20 per cent seem not to have optical counterparts. To get an idea of the energy spectrum of these sources, we construct an X-ray colour–colour diagram using the energy bands 0.3–2, 2–4.5 and 4.5–12 keV. We analyse the spectra of the most intense X-ray sources associated with early-type stars, including the luminous blue variable η Carina and WR25. We show that the X-ray emission from these sources is well fitted by multitemperature model spectra. We detect surprisingly intense X-ray emission at energies above 4 keV for some of the observed early-type stars, especially from CPD-59 2629 (Tr16-22) which presents particularly hard X-ray emission. We detect intense soft X-ray emission, below <2 keV, in HDE 303311, which presents an X-ray excess of about 100 times higher than has been observed in other O5V stars. We use these data to construct the $L_{\rm x}/L_{\rm bol}$ relation for the 0.3–12 and 3.0–12 keV energy ranges, for all the observed O-type stars, plus η Carina and WR25. Most of the bright stars seem to agree with low metallicity spectral models. The $L_{\rm x}/L_{\rm bol}$ ratio for O-type stars in the 0.3–12 keV range is well fitted by a constant $\approx 6.0^{7.5}_{4.8} \times 10^{-7}$, in fair agreement with the canonical expression $L_{\rm x}/L_{\rm bol} \sim 2 \times 10^{-7}$ formerly estimated for the 0.3–2.4 keV energy band. In contrast, the $L_{\rm x}/L_{\rm bol}$ relation for the 3.0–12 keV range presents a strong deviation from the canonical relation, with a high dispersion of about four orders of magnitude. We also detect intrinsic X-ray time variability in seven sources, over the time-scale of about 50 h covered by the observations. This includes an X-ray flare of about 2-h duration detected in DETWC Tr16 J104429.2−594143, a source probably not physically associated with the Carina nebula. We discuss the different underlying physical mechanisms that can be responsible for the X-ray emission from early-type stars.

Key words: H II regions – ISM: individual: NGC 3372 – X-rays: ISM – X-rays: stars.

1 INTRODUCTION

The Carina nebula region (NGC 3372) is one of the most interesting massive star-forming regions in the Galaxy. It harbours the open clusters Trumpler 14 and Trumpler 16 which contain dozens of massive O-type stars, three Wolf–Rayet stars, and the still controversial luminous blue variable (LBV) η Carina.

Surveys made with the *Einstein* observatory two decades ago showed that essentially all OB stars are X-ray emitters in the 0.2–3 keV band (Seward et al. 1979), with luminosities ranging from 10^{32} erg s^{-1} for early O stars, to 10^{28} erg s^{-1} for late B stars, and broadly following the relation $\log(L_{\rm x}/L_{\rm bol}) \approx -7$ or -8.5, respectively (Chlebowski, Harnden & Sciortino 1989).

The first X-ray observation of the Carina nebula made by the *Einstein* observatory in the 0.2–3.5 keV energy range (Seward et al. 1979), and later *ROSAT* Position Sensitive Proportional Counter (PSPC) and High Resolution Imager (HRI) observations in the band 0.2–2.4 keV (Corcoran et al. 1995), allowed the detection of large-scale diffuse emission in the Carina nebula. Most of this emission comes from hot gas at a temperature of about 10^7 K and $n_{\rm e} \sim 0.1$–1 cm^{-3}. The energy to heat this gas probably comes from the strong stellar winds of several early-type stars embedded in the nebula, instead of resolved X-ray sources (Seward & Chlebowski 1982).

Subsequently, in the context of the international X-Mega campaign (Corcoran et al. 1999), the Carina nebula has been observed with *ROSAT* between 1997 December and 1998 January, for a total exposure time of about 47 ks in the soft and medium energy bands

★Fellow of CIC, Prov. de Buenos Aires, Argentina.
†E-mail: nmorrell@lco.cl
‡Member of Carrera del Investigador Científico, CONICET, Argentina.
§Visiting Scientist, Carnegie Institution of Washington, Las Campanas Observatory, Chile.

© 2003 RAS

Table 1. Observing log. The observing revolutions 115 and 116 are identified by the numbers 0112580601 and 0112580701. PFF and PPSF refer to Prime-Full-Frame and Prime-Partial-Small-Frame observing modes, respectively.

EPIC camera	Revolution no	Start time yr/m/d at h:m:s (UTC)	Exposure time (s)	Blocking filter	Observing mode
MOS-1	115	2000/07/26 at 05:07:47	33598	Thick	PFF
MOS-2	115	2000/07/26 at 06:00:45	30497	Thick	PPSF
PN	115	2000/07/26 at 05:48:51	31409	Thick	PFF
MOS-1	116	2000/07/27 at 23:57:54	10867	Thick	PFF
MOS-2	116	2000/07/28 at 00:50:51	7998	Thick	PPSF
PN	116	2000/07/28 at 00:38:57	9216	Thick	FF

(0.2–2.4 keV). Most of the detected X-ray point-like sources were associated with massive early-type stars, which was the starting point of a coordinated optical and X-ray survey of several O-type stars in the region (Albacete Colombo et al. 2001; Morrell et al. 2001; Rauw et al. 2001; Albacete Colombo et al. 2002).

Recently, the Carina nebula region has been observed with the *XMM–Newton* X-ray telescope. The large effective area of the instruments on board *XMM–Newton* provides the deepest observations, at moderate spectral and spatial resolution, of the Carina nebula obtained to date, over the unprecedented broad energy band of 0.3–12 keV. We used these data to make the deepest X-ray source detection, identification and analysis ever carried out in this region, which we present in this paper. In order to better understand the underlying mechanisms and stellar environment responsible for the large differences observed between individual values of $L_{\rm x}/L_{\rm bol}$, we reconstruct this relation for many O-type stars detected as X-ray sources in the region.

2 X-RAY OBSERVATIONS

The Carina nebula field, centred at the position of η Carina ($\alpha_{2000} = 10^{\rm h}45^{\rm m}03\overset{\rm s}{.}4$, $\delta_{2000} = -59^\circ41'03\overset{''}{.}1$), was observed with the *XMM–Newton* satellite in two separate revolutions (115 and 116) between 2000 July 26 and 28. The observations were not affected by high flaring background fluxes, giving a good time interval ($\approx$44 ks) of useful exposure time (Table 1). The observatory consists of three X-ray telescopes, as described by Jansen et al. (2001). Data were acquired with the European Photon Imaging Camera (EPIC), which provides simultaneous CCD imaging spectroscopy from the PN camera (Strüder et al. 2001) and two identical MOS cameras, MOS-1 and MOS-2 (Turner et al. 2001)). Full-frame mode and the thick blocking filter were used in order to reject optical light. These two conditions apply only to the PN and MOS-1 cameras, which provide a field of view of $\approx$30 arcmin in diameter and energy coverage from $\approx$0.2 to 15 keV at medium energy resolution ($E/\Delta E \approx 20$–50) and $\approx$12-arcsec FWHM angular resolution.

Data reductions followed standard procedures using the version 5.3 of the *XMM–Newton* Science Analysis System software (SAS v5.3).[1] The pipeline processing tasks EMCHAIN and EPCHAIN were executed using the latest calibration files and the data were filtered with EVSELECT to choose good event patterns. Spectra and light curves were extracted from the filtered events using circular regions of different radii for the most intense sources in the observed field. Data from the MOS-1 and PN cameras for different revolutions were combined in order to increase the signal-to-noise (S/N) ratio, thus reducing uncertainties in parameters derived from the spectral fits. Spectra were analysed with XSPEC version 11.2 (Arnaud 1996).

3 X-RAY IMAGES

The X-ray image obtained by *XMM–Newton* gives us the possibility of obtaining the deepest X-ray source detection ever carried out in the 0.3–12 keV energy range, in the Carina nebula. In Fig. 1 we show a region of $\approx$30 arcmin around η Carina, comprising the open clusters Trumpler 14 and Trumpler 16, as observed with the PN and MOS-1 (full frame, exposure corrected image).

Because of the strong noise affecting the PN and MOS-1 detectors below 0.3 keV, and the uncertain calibration of the EPIC instruments at low energies, we ignored all energy channels below 0.3 keV. It should also be noted that the sensitivity of *XMM–Newton* above 12 keV drops to less than 25 per cent of that at 10 keV, and so we decided to limit the high-energy range to a maximum value of 12 keV.

To correct for differences in exposure and vignetting of different parts of the images we divided each image by an exposure map using the EEXPMAP[2] routine. We did this in three different energy bands, the soft (0.3–2 keV), medium (2–4.5 keV) and hard (4.5–12 keV) bands. We selected the bands such that the instrument effective areas are approximately equal in each band.

The colour image in Fig. 1 is the combination of the soft (red), medium (green) and hard (blue) energy bands. This image is useful to obtain a rough estimate of the hardness of the X-ray radiation of each detected source, which in turn provides an idea of the physical mechanism responsible for the X-ray emission. The fact that some sources are brighter in the soft bands, whereas others are brighter in the hard bands, suggested to us the possibility of carrying out an independent search of sources over the soft, medium and hard energy bands.

3.1 Source detection and identification

We searched the high-resolution images provided by the *XMM–Newton* observation using two tasks available in SAS v5.3: the *sliding cell detection and maximum likelihood* (ML) method EMLDETECT (Cash 1979) and the *wavelet detection* routine EWAVELET (Micela et al. 1997).

In order to detect as many X-ray sources as possible in the observed region, we applied both methods to data from the whole energy band (0.3–12 keV) and independently to each of the three (soft, medium and hard) energy bands defined above.

[1] See http://xmm.vilspa.esa.es/user

[2] See http://xmm.vilspa.esa.es/sas/current/doc/eexpmap/index.html

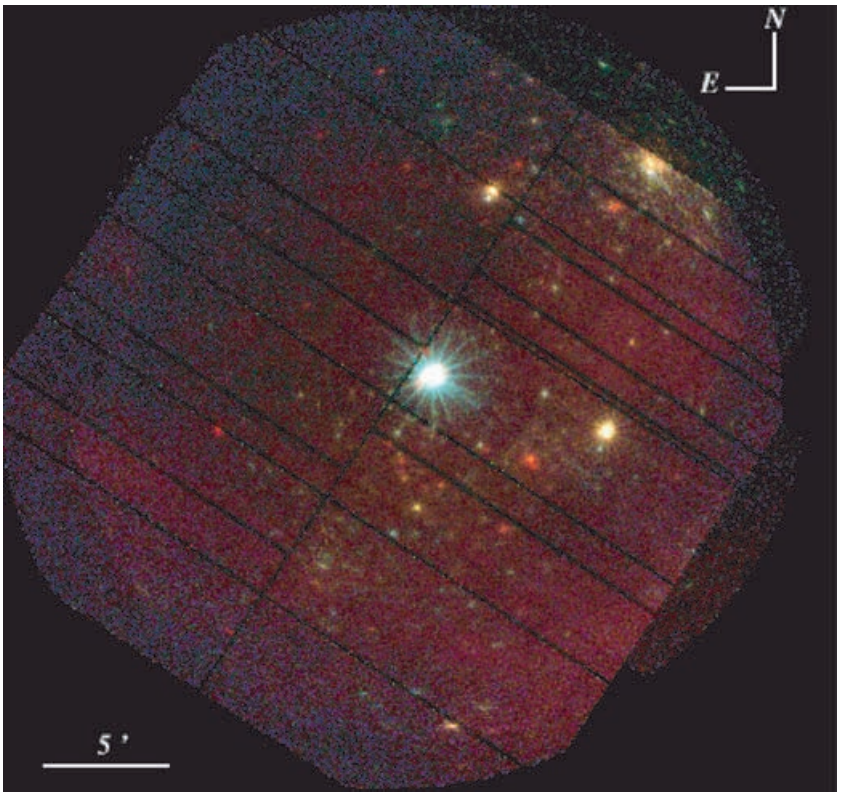

Figure 1. X-ray colour image of the the Carina nebula from the combined MOS-1 and PN detectors; exposure-map corrections have been applied to the individual images before combining them. The image is centred in the η Carina sky position ($\alpha_{2000} = 10^{\rm h}45^{\rm m}03\overset{\rm s}{.}80$, $\delta_{2000} = -59^\circ41'05\overset{''}{.}4$). The horizontal and vertical axes correspond to right ascension and declination, respectively. Different colours represent different X-ray energy bands: red, 0.3–2 keV; green, 2–4.5 keV; blue, 4.5–12 keV.

The sliding cell detection method consists of simple sliding window box detection algorithms which uses a low S/N ratio ($\sim 4\sigma$) above the background in order to have as many objects as possible in the input for the ML method. A local background map is derived from images smoothed by a two-dimensional (2D) spline function, after the bright sources have been removed, using the ESPLINEMAP task, keeping the source position fixed for all the energy bands while adding the source existence likelihoods from the individual energy bands together. We found about 100 sources detected simultaneously in the MOS-1 and PN images with a combined logarithm likelihood limit

$$L = -(\ln(P_{\rm mos-1}) + \ln(P_{\rm pn})) \geqslant 10, \quad (1)$$

where P represents the probability that the observed counts in the image come from random Poissonian fluctuation instead of a real source. However, this method requires a point spread function (PSF) model to perform the likelihood calculation, and thus favours the detection of point-like sources, failing in the detection of extended sources because of their splitting. Extensive likelihood could be reliably applied only for bright sources; it cannot detect objects which are not already present in the input list (e.g. missing detections in the local or map phases will be lost). Another serious drawback of this method is the relatively large number of spurious detections over CCD gaps.

A better source detection was possible by an extension of the Fourier transform based on the wavelet decomposition algorithm, using the mathematical properties of the wavelet function, often the second derivative of the 2D Gaussian function, or so-called 'Mexican hat' (MH).

This wavelet technique (WT) decomposes the original X-ray image into a given number of wavelet images (w_a), within the chosen set of scales a, which are distributed normally over a Gaussian white noise image. This is not strictly correct for X-ray images where Poissonian photon noise dominates, and therefore several techniques have been developed that allow selecting the significant wavelet coefficients in X-ray images (Vikhlinin, Forman & Jones 1997; Vikhlinin, Pierre & Gastaud 2001).

The control parameters which need attention are the significance threshold, the set of scales and the number of iterations. In order to obtain a well-defined image convolution, and also to be more sensitive and less affected by source confusion, we use a significance threshold of 10^{-4}, corresponding to one false event in 10 000 ($\approx 4\sigma$), a wavelet scale of $1/16$, and we run three iterations for each image.

For all the sources detected in our images, the errors in source position are dominated by residual systematic errors of the order of 2–5 arcsec. The count rates were estimated by convolution of an input image divided by the exposure map, with the MH wavelet, which is better for point-like source detection and count rate estimation than the ML method. The photometry is accurate to within 10 per cent for point-like sources, and near to 20 per cent for blended sources, where these uncertainties can be regarded as intrinsic errors due to the Poissonian nature of the X-ray images (Vikhlinin et al. 2001). However, random Poissonian fluctuations still might produce spurious detections. We solved this problem by a careful inspection to manually reject such spurious detections (e.g. hot pixels).

We finally kept 80 X-ray source detections within the field covered by the combined MOS-1 and PN image (Fig. 2). The different

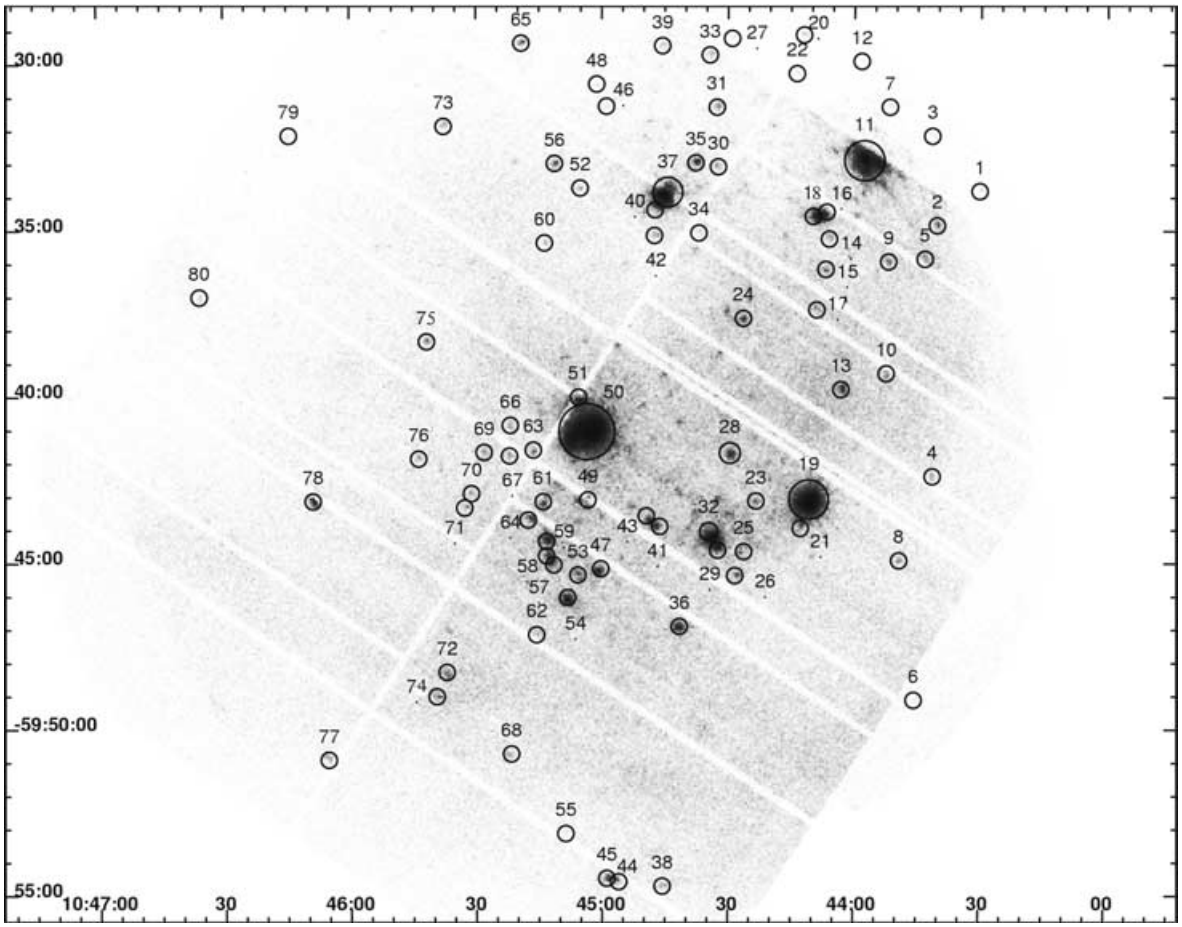

Figure 2. Source detection in the combined MOS-1 and PN (0.3–12 keV) X-ray image. All sources detected above a 4σ confidence level are indicated with circles. The horizontal and vertical axes represent α_{2000} and δ_{2000}, respectively.

image size between MOS-1 and PN CCD images, along with dead columns and bad pixels, caused some sources to be detected only in one camera. The detected X-ray sources are listed in Table 2 in order of increasing right ascension, labelled with our own numbering followed by the source designation according to the naming conventions recommended by the *XMM* Science Operations Centre (SOC) and the International Astronomical Union.[3] Other identifications for those sources are also provided, namely HD#, CPD#, MJ# (Massey & Johnson 1993), Y# (Cudworth, Martin & DeGioia-Eastwood 1993), Tr14/16# (Feinstein, Marraco & Muzzio 1973), DETWC (DeGioia-Eastwood et al. 2001), and GSC2.2. The visual magnitudes and spectral types quoted in Table 2 were obtained from the SIMBAD data base.

Spectral classification is lacking for about 60 per cent of the detected X-ray sources. Among these, 15 sources have not been optically identified. With the aim of finding out about the physical nature of those X-ray sources we looked for a possible correlation between X-ray fluxes and visual magnitudes (when available) without any positive results. A plausible explanation for this fact lies in the possibility that most of those unidentified X-ray sources could be associated with foreground/background late-type stars with coronal activity. An alternative interpretation, finding support in Zinnecker & Preibisch (1994) and Feigelson et al. (2002), is that soft X-ray emission can be associated with intermediate mass Herbig Ae/Be stars, representing some of the youngest objects in this star-forming region. These authors report for such sources luminosities between 10^{30} and 10^{32} erg s^{-1}, which agree with the X-ray fluxes estimated for several X-ray sources in our sample. A further spectroscopic investigation of unidentified sources is presently in progress.

For comparison, we mention that Evans et al. (private communication) detected 180 X-ray sources in the Carina nebula, analysing observations obtained in the soft energy band (0.5–2.04 keV) with the ACIS-I instrument on board *Chandra*. However, *Chandra* has much higher spatial resolving power (≈5 arcsec) than *XMM–Newton* (≈15 arcsec), while the latter gives well-calibrated information from the MOS and PN cameras on a broader spectral region ($E/\Delta E \approx 50$, compared to $E/\Delta E \approx 10$ for the ACIS camera). Besides, the *Chandra* data discussed by Evans et al. (private communication) were difficult to calibrate due to charged particle damage occurring during the observations.

3.2 X-ray count rates and fluxes

We used the images in the three energy bands to calculate the X-ray colours of the detected sources. Each X-ray band was selected to reflect a spectral characteristic of the source: the soft (S) band includes several emission lines from C, N, O and Ne below 2 keV; the medium (M) band is dominated by continuum radiation; the hard (H) band includes, at least, the Fe XXVI 6.4-keV line.

[3] *XMM–Newton* Newsletter No. 4, 2001 April.

Table 2. X-ray sources detected in the Carina nebula. The first and second columns give our identification and that recommended by the *XMM* SOC and the IAU for serendipitous *XMM–Newton* source detections. Columns 3 and 4 give J2000 coordinates on the X-ray image. Columns 5, 6 and 7 provide cross-identifications, spectral type and visual magnitude, respectively. Spectral types and visual magnitudes were obtained from Massey & Johnson (1993). A ‡ is used to label sources that are not resolved in the X-ray image. References are denoted as: DETWC (DeGioia-Eastwood et al. 2001); MJ (Massey & Johnson 1993); Y (Cudworth et al. 1993); GSC2.2 (*HST* Guide star Catalog v2.2.01).

Source	XMMUJ	X-ray position		Optical nomenclature	Spectral	V
	I.d	α_{2000} (h:m:s)	δ_{2000} (°:′:″)	hd/cpd/Ref.	type	
1	104329.8-593344	10:43:29.88	−59:33:44.2	Unknown	–	–
2	104339.9-593445	10:43:39.97	−59:34:45.6	DETWC Tr 14 J104339.8-593445	–	15.43
3	104341.3-593205	10:43:41.35	−59:32:05.6	DETWC Tr 14 J104341.3-593205	–	15.72
4	104341.4-594223	10:43:41.40	−59:42:23.8	Unknown	–	–
5	104343.5-593545	10:43:43.54	−59:35:46.5	Tr14 MJ 103/Tr14-61	–	13.53
6	104343.9-594901	10:43:43.94	−59:49:01.6	Unknown	–	–
7	104349.7-593115	10:43:49.79	−59:31:15.4	Unknown	–	–
8	104349.8-594453	10:43:49.81	−59:44:53.0	Cl* Tr14 Y 334	–	14.34
9	104352.1-593556	10:43:52.13	−59:35:55.5	DETWC Tr14 J104352.1-593556	–	16.58
10	104352.3-593924	10:43:52.02	−59:39:24.3	GSC2.2-S11303023021	–	16.4 (R)
11‡	104354.3-593257	10:43:54.29	−59:32:57.3	HD 93128	O3V((f))	8.84bl
11‡	104356.7-593252	10:43:56.73	−59:32:52.7	Cl Tr14 1	–	6.97bl
11‡	104357.5-593253	10:43:57.52	−59:32:53.1	HD 93129AB	O3If*	6.90bl
12	104358.3-592952	10:43:58.25	−59:29:52.0	DETWC Tr14 J104358.2-592952	–	17.30
13	104402.9-593946	10:44:02.92	−59:39:46.4	Cl* Tr14 Y 442	–	13.49
14	104405.9-593512	10:44:05.91	−59:35:12.4	Cl* Tr16 MJ 224/Tr16-124	B1V	11.19bl
15	104406.9-593612	10:44:06.87	−59:36:11.9	Cl* Tr14 MJ 228	–	13.29
16	104407.1-593428	10:44:07.07	−59:34:28.9	HD 93160	O6III(f)	7.88bl
17	104409.9-593433	10:44:09.93	−59:34:33.4	HD 93161AB	O6.5((f))V	7.87bl
18	104409.9-593723	10:44:09.99	−59:37:23.0	Unknown	–	–
19‡	104410.3-594311	10:44:10.62	−59:43:13.5	HD 93162/WR25	WN7+abs	8.11
19‡	104413.1-594311	10:44:13.18	−59:43:11.1	Tr16-244	O3I	10.80
20	104411.7-592907	10:44:11.77	−59:29:07.2	Unknown	–	–
21	104413.2-594311	10:44:13.28	−59:43:11.1	Unknown	–	–
22	104413.5-593016	10:44:13.50	−59:30:16.8	Unknown	–	–
23	104423.2-594311	10:44:23.25	−59:43:11.3	Unknown	–	–
24	104425.9-593740	10:44:25.94	−59:37:40.7	Unknown	–	–
25	104426.9-594437	10:44:26.90	−59:44:37.6	Unknown	–	–
26	104427.9-594521	10:44:27.92	−59:45:21.8	Cl* Tr16 MJ 317	–	10.12
27	104428.3-592911	10:44:28.33	−59:29:11.8	Unknown	–	–
28	104429.2-594143	10:44:29.05	−59:41:43.2	DETWC Tr16 J104429.2-594143	–	15.21
29	104432.3-594431	10:44:32.14	−59:44:29.7	HD 93204	O5V	8.48
30	104432.8-593302	10:44:32.81	−59:33:02.4	Cl* Tr 16 MJ 332	–	14.04
31	104432.9-593118	10:44:32.88	−59:31:18.0	GSC2.2-S111303026995	–	–
32	104433.7-594415	10:44:33.62	−59:44:14.8	HD 93205	O3V+O8V	7.76
33	104434.0-592946	10:44:34.04	−59:29:46.7	Unknown	–	–
34	104436.2-593517	10:44:36.27	−59:35:17.3	Cl* Tr14 MJ 349	–	11.79
35	104437.4-593255	10:44:37.44	−59:32:53.8	HDE 303311	O5V	8.90
36	104441.9-594657	10:44:41.90	−59:46:57.7	CPD-59 2600/Tr16-100	O5.5V	8.52
37	104444.8-593354	10:44:44.87	−59:33:54.7	HD 93250/Tr16-101	O3((f))V	7.41
38	104445.3-595443	10:44:45.31	−59:54:43.2	HDE 305524/Cr228 7	O6Vn	9.32
39	104445.3-592925	10:44:45.33	−59:29:25.0	GSC2.2-S11303027729	–	15.90(R)
40	104446.5-593413	10:44:46.33	−59:34:14.6	Cl*Tr 14 MJ 394	–	13.23
41	104447.1-594355	10:44:47.11	−59:43:55.0	CPD-59 2603/Tr16-104	(O7V+O9V)+B1.5V	8.75bl
42	104447.7-593508	10:44:47.72	−59:35:08.7	GSC2.2-S11303025187	–	16.92(R)
43	104448.8-594342	10:44:48.83	−59:43:42.0	DETWC Tr 14 J104449.0-594340	–	16.76
44	104457.4-595430	10:44:57.46	−59:54:30.1	Cl*Cr228 #113	–	11.44
45	104457.9-595434	10:44:57.90	−59:54:34.5	Unknown	–	–
46	104458.4-593115	10:44:58.40	−59:31:15.1	Unknown	–	–
47	104501.1-594515	10:45:01.24	−59:45:15.8	Cl* Tr14 Y 230	–	14.56
48	104501.2-593036	10:45:01.21	−59:30:36.1	Unknown	–	–
49	104503.0-594302	10:45:03.23	−59:43:02.8	Unknown	–	–
50	104503.8-594105	10:45:03.80	−59:41:05.4	η Carina	LBV	6.21V
51	104504.8-594004	10:45:04.89	−59:40:04.5	HDE 303308/Tr16-7	O3((f))V	8.21
52	104504.9-593346	10:45:04.90	−59:33:46.0	GSC2.2-S11303025851	–	16.65(R)
53	104505.8-594519	10:45:05.85	−59:45:20.1	CPD-59 2626/Tr16-23	O7V	10.00
54	104508.3-594605	10:45:08.30	−59:46:05.5	CPD-59 2629/Tr16-22	O8.5V	10.93
55	104508.4-595309	10:45:08.19	−59:53:11.5	Unknown	–	–
56	104511.2-593258	10:45:10.95	−59:32:58.2	Cl* Tr14 Y 82	–	13.62

Table 2 – *continued*

Source	XMMUJ I.d	X-ray position α_{2000} (h:m:s)	X-ray position δ_{2000} (°:′:″)	Optical nomenclature hd/cpd/Ref.	Spectral type	V
57	104512.4-594500	10:45:12.43	−59:45:02.3	HD 93343/Tr16-182	O7V(n)	9.58
58	104512.7-594447	10:45:12.75	−59:44:45.3	CPD-59 2635/Tr16-34	O7V+O8V	9.43
59	104512.9-594420	10:45:12.75	−59:44:19.2	CPD-59 2636/Tr16-110	(O7V+O8V)+O9V	9.17
60	104513.2-593524	10:45:13.25	−59:35:24.1	GSC2.2-S11303041403	–	15.89(R)
61	104514.0-594316	10:45:14.00	−59:43:16.2	GSC2.2-S11303039419	–	17.14(R)
62	104514.5-594708	10:45:14.50	−59:47:08.8	Unknown	–	–
63	104516.2-594140	10:45:16.23	−59:41:40.3	Cl* Tr16 MJ 531/Tr16-238	–	13.57
64	104516.4-594337	10:45:16.45	−59:43:37.6	CPD-59 2641/Tr16-112	O6V((f))	9.22
65	104519.1-592920	10:45:19.17	−59:29:20.6	GSC2.2-S11303027782	–	13.85
66	104521.6-594052	10:45:21.60	−59:40:52.2	DETWC Tr16 J104522.0-594052	–	16.98
67	104522.0-594146	10:45:22.00	−59:41:46.0	GSC2.2-S113033021845	–	15.49(R)
68	104522.3-595048	10:45:22.29	−59:50:48.2	Cl* Tr16 MJ 568	–	11.29
69	104527.9-594140	10:45:27.93	−59:41:40.0	DETWC Tr 16 J104528.0-594139	–	16.01
70	104531.8-594252	10:45:31.71	−59:42:52.0	Tr 16 J104531.8-594252	–	16.92
71	104532.1-594318	10:45:32.12	−59:43:18.4	Unknown	–	–
72	104536.4-594823	10:45:36.42	−59:48:22.5	Cl* Tr16 MJ 596/FO 15	O4:5V	12.10
73	104537.2-593146	10:45:37.25	−59:31:46.3	GSC2.2-S11303026767	–	16.26(R)
74	104538.0-594901	10:45:38.00	−59:49:01.5	Unknown	–	–
75	104541.6-593819	10:45:41.66	−59:38:19.8	GSC2.2-S11303023625	–	14.78(R)
76	104543.1-594150	10:45:43.19	−59:41:50.9	GSC2.2-S11303021789	–	–
77	104605.7-595049	10:46:04.76	−59:50:54.0	Cl* Cr228 # 98	–	10.03
78	104608.1-594306	10:46:08.15	−59:43:06.0	Unknown	–	–
79	104609.5-593209	10:46:09.01	−59:32:09.7	Unknown	–	–
80	104635.7-593700	10:46:35.26	−59:37:06.3	HDE 303304	O+?	9.71

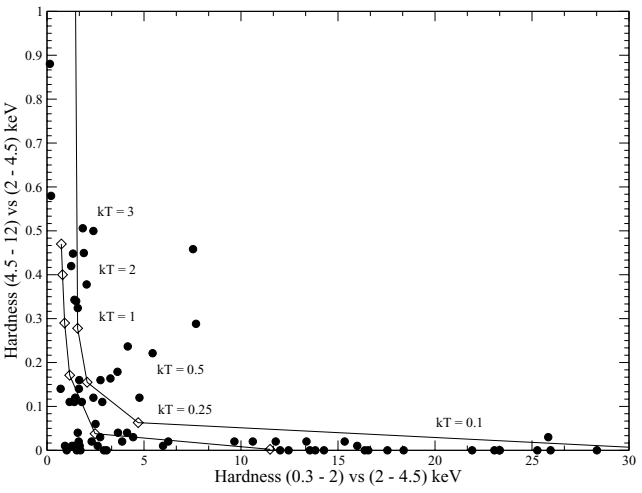

Figure 3. X-ray colour–colour diagram of the sources detected in the combined PN/MOS-1 image. The colours are defined as the count rate ratio in the 4.5–12 and 2–4.5 keV bands (*y*-axis), and the 0.3–2 and 2–4.5 keV bands (*x*-axis), respectively. The upper and lower curves show the location of models for thermal plasma RAYMOND (Raymond & Smith 1977) with temperatures $kT = 0.1$, 0.25, 0.5, 1, 2 and 3 keV, using hydrogen column densities $N_{\rm H}$ of 0.45 and 0.90×10^{22} cm^{-2}, respectively.

Hence, the hardness of each source, i.e. the count rate ratio between two energy bands, provides a rough way of identifying the emission mechanism that dominates the radiation spectrum of each source. In Fig. 3 we plot the count ratios H/M versus S/M for every detected source.

In order to convert the observed count rates into energy fluxes expressed in erg cm^{-2} s^{-1} ([cgs] units) for each detected X-ray source, we extracted pulse-height spectra of the brightest sources listed in Table 3 that we fitted using different models (see Section 4). We then used these models to simulate spectra of sources at different flux levels on the image, and from these we calculated the expected count rates. We repeated this procedure until we covered the whole range of count rates observed in the X-ray image. We find the following relations between detected count rates and observed fluxes (F) in the 0.3–12 keV range for the PN and MOS-1 cameras, respectively:

$$F_{\rm pn} = 5.78 \times 10^{-12}\,({\rm counts\,s^{-1}}) + 1.4 \times 10^{-14}\,[{\rm cgs}], \quad (2)$$

$$F_{\rm mos-1} = 1.34 \times 10^{-11}\,({\rm counts\,s^{-1}}) + 9.0 \times 10^{-15}\,[{\rm cgs}]. \quad (3)$$

Finally, we used the average value of $N_{\rm H}$ from our spectral fits (see below) to calculate unabsorbed X-ray fluxes ($F^{\rm o}$). These relations are as follows:

$$F^{\rm o}{}_{\rm pn} = 3.8(F_{\rm pn}) + 5.6 \times 10^{-14}\,[{\rm cgs}], \quad (4)$$

$$F^{\rm o}{}_{\rm mos-1} = 3.7(F_{\rm mos-1}) + 2.4 \times 10^{-14}\,[{\rm cgs}]. \quad (5)$$

The faintest sources in this region have about 1×10^{-3} and 3×10^{-3} counts s^{-1} over the 0.3–12 keV band for the MOS-1 and PN images, respectively. From the correlation between count rates and energy flux above, and assuming a 1-keV thermal spectrum with a neutral hydrogen column density $N_{\rm H} \approx 0.5 \times 10^{22}$ cm^{-2}, the faintest detected sources in both cameras correspond to an observed flux of about 0.1×10^{-13} erg cm^{-2} s^{-1}.

To get an idea of the spectral energy distribution for the detected X-ray sources, we calculated X-ray colours for them and plotted those along with thermal emission plasma models obtained for two interstellar absorption hydrogen column densities $N_{\rm H} = 0.45$ and 0.90×10^{22} cm^{-2}, respectively. As Fig. 3 shows, most of the X-ray sources follow a thermal emission plasma spectrum model

Table 3. Spectral parameters derived for the brightest observed X-ray sources. Fitted models are combinations of multiple thermal emission (RAY; Raymond & Smith 1977) and blackbody (BB) models. The flux was estimated for the 0.3–12 keV energy range, and the column density ($n_{\rm H}$) is expressed in units of 10^{22} cm^{-2}. A † refers to X-ray spectra affected by dead columns or CCD gaps in at least one of the EPIC images.

Source Name	Model Id.	$n_{\rm H}$ $\times 10^{22}$ cm^{-2}	Temperature [keV]	Ab.-Ion [Fe/H]	Reduced χ^2/d.o.f.	Count rate $\times 10^{-3}$ MOS-1	Count rate $\times 10^{-3}$ PN	X-ray flux $\times 10^{-13}$ [cgs] Absorbed	X-ray flux $\times 10^{-13}$ [cgs] Unabsorbed
η Carina	RAY	0.69 ± 0.03	0.04 ± 0.01	0.45 ± 0.08	1.1/2031	2760 ± 9	8822 ± 18	793 ± 9	16510 ± 800
	RAY	0.29 ± 0.01	0.78 ± 0.06	0.45 ± 0.08					
	RAY	5.13 ± 0.06	1.25 ± 0.03	0.45 ± 0.08					
	RAY	10.5 ± 0.4	4.40 ± 0.06	0.45 ± 0.08					
	LINE		0.68 ± 0.02	O VII					0.61 ± 0.08
	LINE		6.47 ± 0.02	Fe K					13.1 ± 0.2
WR 25	RAY	0.81 ± 0.02	0.76 ± 0.08	0.54 ± 0.04	1.0/845	543 ± 4	1163 ± 6	76.1 ± 0.9	256.3 ± 0.3
	RAY	0.38 ± 0.02	3.1 ± 0.1	0.54 ± 0.04					
	LINE		0.72 ± 0.04	O VII					0.20 ± 0.09
HDE 303311	RAY	0.88 ± 0.06	0.14 ± 0.05	1.0 ± 0.8	0.9/51	–	38 ± 2	0.9 ± 0.1	112 ± 20
HD 93205	RAY	0.45 ± 0.06	0.25 ± 0.01	0.6 ± 0.3	1/229	49 ± 1	155 ± 2	6.4 ± 0.3	35 ± 2
	RAY	0.20 ± 0.08	0.97 ± 0.06	0.6 ± 0.3					
HD 93250†	RAY	0.26 ± 0.09	0.81 ± 0.02	0.13 ± 0.06	1.0/375	201 ± 1	226 ± 3	21 ± 5	34 ± 2
	RAY	0.23 ± 0.04	5 ± 1	0.13 ± 0.06					
CPD-59 2629	RAY	1.2 ± 0.1	0.37 ± 0.07	0.8 ± 0.3	1/129	15.7 ± 0.8	40 ± 1	2.8 ± 0.3	30 ± 1
	RAY	0.4 ± 0.2	2.5 ± 0.3	0.8 ± 0.3					
HDE 303308†	RAY	0.56 ± 0.1	0.23 ± 0.04	0.4 ± 0.5	0.8/92	17.6 ± 0.9	–	3.5 ± 0.4	25 ± 2
	BB	0.1 ± 0.1	1.6 ± 0.5	0.4 ± 0.5					
HD 93161	RAY	0.5 ± 0.1	0.22 ± 0.03	0.8 ± 0.8	0.9/80	–	31 ± 2	2.2 ± 0.4	17.8 ± 0.8
	RAY	0.5 ± 0.2	0.9 ± 0.1	0.8 ± 0.8					
HD 93204	RAY	0.36 ± 0.07	0.29 ± 0.03	0.3 ± 0.2	0.9/81	–	26 ± 3	1.3 ± 0.3	10.2 ± 0.7
CPD-59 2600	RAY	0.4 ± 0.04	0.30 ± 0.01	0.18 ± 0.07	1.0/94	8.2 ± 0.6	27 ± 1	1.1 ± 0.2	8.8 ± 0.3
CPD-59 2603	RAY	0.5 ± 0.1	0.29 ± 0.06	0.2 ± 0.3	1.1/70	–	14 ± 1	0.5 ± 0.1	5.4 ± 0.7
CPD-59 2641†	RAY	1.2 ± 0.8	0.3 ± 0.2	0.3 ± 0.4	1.0/63	–	4 ± 1	0.2 ± 0.1	5.3 ± 0.8
HD 93160	RAY	0.18 ± 0.04	0.69 ± 0.04	0.11 ± 0.03	0.9/61	–	19 ± 2	1.6 ± 0.2	3.2 ± 0.6
FO 15	RAY	0.4 ± 0.1	3.2 ± 0.7	0.8 ± 0.5	0.9/61	–	11 ± 1	1.1 ± 0.1	1.7 ± 0.3

with temperatures between 0.1 and 0.5 keV. For the brightest sources, an important amount of the total X-ray energy is emitted in the medium and hard bands, and they match more or less the relation determined by temperatures of about 1–4 keV. Several X-ray sources lie in between both relations, indicating a combination of the two absorption values. The locations of some X-ray sources above both relations may be indicative of the presence of an extra absorption column component.

4 X-RAY SPECTRA

We extracted individual PN and MOS-1 pulse-height spectra, background corrected the spectra, and built the corresponding redistribution matrices and ancillary response files for the brightest X-ray sources detected in the image (see Table 3). The spectra were rebinned so that they have a minimum of nine counts per channel and were analysed using XSPEC version 11.2.

Previous observations have indicated that the X-ray emission from early-type stars is consistent with thermal plasma models for temperatures between 3–9 $\times$ 10^6 K, or $kT \approx 0.25$–0.75 keV (Chlebowski et al. 1989).

We fitted the PN and MOS-1 spectra simultaneously using single-temperature and multiple-temperature thermal plasma models (Raymond & Smith 1977), combined with a multiplicative photoelectric absorption model based on the cross-sections from Morrison & McCammon (1983).

Parameters for the best-fitting models are listed in Table 3 where, in some cases, the low number of detected photons allowed us only to derive lower limits for the plasma temperature, leaving room for relatively large uncertainties in the derived spectral parameters.

As can be seen in Table 3, the fits suggest a low metallicity in the region, varying between 0.2 and 0.7 times of solar abundance. This is not likely the case for the Carina nebula region, and in fact this could be explained by means of the resonance scattering process, in which photons from resonance lines are highly absorbed in the X-ray plasma, leading to underestimation of the abundances of certain elements (Tanaka et al. 1998).

In Fig. 4 we present the fitted EPIC PN spectrum and residual model for the WN6ha+O4f star HD 93162 (=WR 25; van der Hucht 2001). The model consists of a combination of two optically thin emission plasmas. First we tried single-temperature models, which did not provide a good fit to the data – reduced $\chi^2 \geqslant 4.9$ for 848 degrees of freedom (d.o.f.). We then tried to fit the spectrum using a two-temperature model with solar abundance allowing different column densities for both components, but this procedure did not improve the fit enough – reduced $\chi^2 \approx 1.2$ for 848 d.o.f. We finally allowed for abundances lower than solar, obtaining the final fit (reduced $\chi^2 \approx 1.0$ for 848 d.o.f.) presented in Fig. 4. The residuals show an apparent excess probably due to the O VII lines near 0.7 keV. We tried to fit this spectral feature with a Gaussian line in the 0.718–0.724 keV range following Raassen et al. (private communication), in their determination of the thermal structure and elemental composition of the corona of WR 25. We obtained an X-ray flux for line and continuum of about 0.2×10^{-13} and 0.046×10^{-13}, respectively, in cgs units, and a line equivalent width of 4.3 keV. However, this new model did not improve the goodness of the fit (reduced $\chi^2 = 1.03$, d.o.f. = 845) probably due to the low S/N ratio in the soft X-ray energies ($\leqslant$1 keV), and thus we decided to keep the simpler fit presented in Fig. 4.

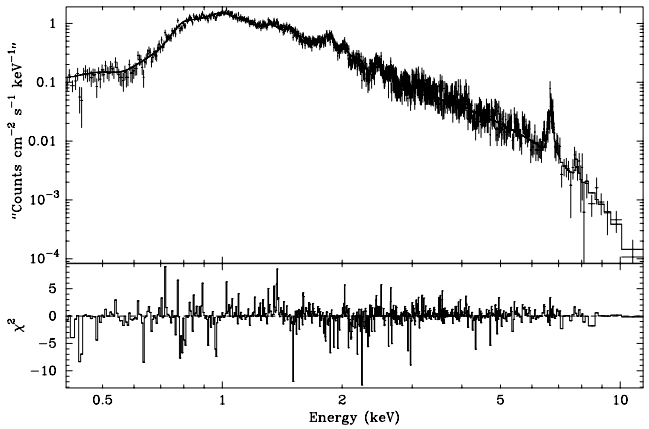

Figure 4. EPIC PN spectrum of HD 93162 (WR 25). The solid line shows the best fit obtained with two thermal models (Raymond & Smith 1977), independently combined with a multiplicative absorption law WABS (Morrison & McCammon 1983). The spectrum clearly shows the 6.7-keV Fe XXV Kα emission line present in the assumed model, which is consistent with the radiative wind shock model.

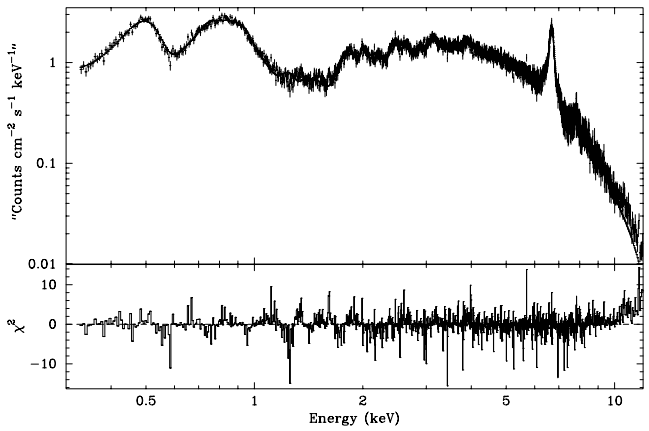

Figure 5. EPIC PN spectrum of η Carina over the 0.3–12 keV energy range. The solid line shows the best fit obtained with four thermal models (Raymond & Smith 1977), which were combined independently with a multiplicative absorption law WABS (Morrison & McCammon 1983). The model includes two Gaussian profiles centred at 0.7 and 6.4 keV in order to fit the O VII and Fe K fluorescent lines, respectively.

What attracted our attention is the relatively large X-ray emission of WR 25, whose luminosity ratio $L_{\rm x}/L_{\rm bol} \sim 2.3 \times 10^{-6}$ is about two orders of magnitude larger than the other two bright WR stars in this region: WR 22 (HD 92740, WN7h+O9III-V) and WR 24 (HD 93131, WN6ha) (Wessolowski 1996). Several interpretations were proposed for this abnormally high X-ray flux (e.g. phase of transition between O-type and WR). However, Maeda & Tsuboi (1999), analysing data from the *Chandra* X-ray telescope, found an emission line spectrum from highly ionized gas the results of which are consistent with the radiative wind shock model.

In order to fit the X-ray spectrum of η Carina over the 0.3–12 keV range (see Fig. 5), we take into account the different spatial regions in which the soft and hard X-ray radiation originate. This fact is easily observed on the PN colour-energy coded image (Fig. 6), which is similar to that previously published by Corcoran et al. (2001). We mainly observe there two X-ray emission regions: a highly non-uniform soft elliptical shell emission region, which looks brighter

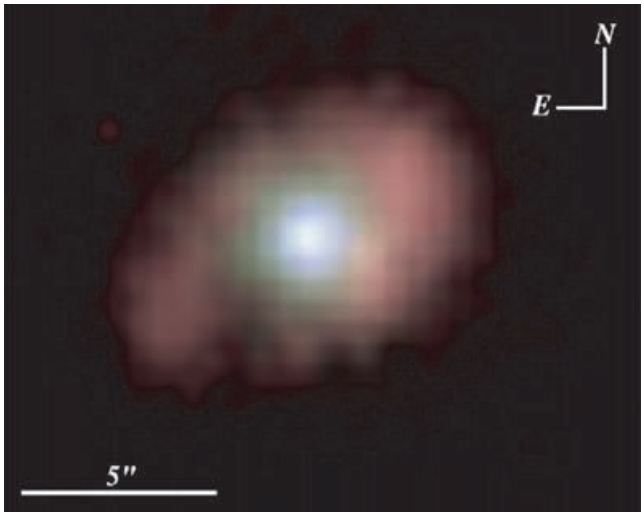

Figure 6. EPIC PN image of η Carina colour coded for X-ray energies as follows: red, 0.3–2 keV; green, 2–4.5 keV; blue, 4.5–12 keV. The soft thermal component is primarily produced by an elliptical ring at a distance of about 10–15 arcsec from the hard component which is dominated by the emission originating within 0.5 arcsec of the star.

to the south-west and fainter to the north-east, and a hard X-ray core, which is unresolved in the EPIC PN image.

The extracted EPIC PN spectrum of η Carina showed two bumps apparently originated in the particular geometry of the elliptical shell (see Fig. 6). We fitted a four-temperature thermal plasma model ($\chi^2 \approx 1.2$ for 2037 d.o.f.) with temperatures $kT \approx 0.04 \pm 0.01$, 0.78 ± 0.06, 1.25 ± 0.03 and 4.40 ± 0.06 keV. The two cooler components dominate the spectrum below 2 keV, whereas the two hotter components agree with the model proposed by Lautenegger, Kahn & Ramsay (2003), and dominate the spectrum over the 2–12 keV range. On this subject, from our fits we estimate that the unabsorbed flux in the 0.3–12 keV range is about 1.65×10^{-9} erg cm^{-2} s^{-1} (see Table 3). These results are in agreement with Corcoran et al. (2001), who found that the unresolved X-ray emission from η Carina requires a non-isothermal temperature distribution to be fitted.

The four-temperature thermal plasma model fit to the η Carina X-ray spectrum still showed large excess emission near 0.7 and 6.4 keV, attributable to the O VII lines near 0.68 keV and the Fe K fluorescent line (Corcoran et al. 1998, 2000), respectively. We then included two Gaussian lines at these positions in our fit, obtaining an overall reduction of χ^2 of 496 from our previous best-fitting value, which means that these lines are detected at a confidence level $\geqslant$99 per cent. The O VII lines near 0.68 keV yield an energy flux of 0.61×10^{-13} erg s^{-1} cm^{-2} related to an equivalent width $\mathrm{EW_{O\,VII}} = 4.37$ keV. The intense feature at 6.7 keV is then produced by a thermal line present in the Raymond–Smith model, and the Fe K fluorescent emission at 6.47 keV. This fluorescent line is produced by scattering of photons from the stellar source, and so in theory offers another diagnostic about the conditions of the X-ray emitting region. As noted by Corcoran et al. (1998), the equivalent width of the Fe K fluorescent line is in general related to the column density of scatterers by the relation $\mathrm{EW} \approx 2.3 N_{24}$ keV, where N_{24} is the total column density of cold material in 10^{24} units (Kallman 1995). For the 6.175–6.775 keV energy range of the η Carina spectrum, the Fe K fluorescent line and the continuum show a flux of about 13.1×10^{-13}, and 102.4×10^{-13} erg s^{-1} cm^{-2}, corresponding to a line equivalent width $\mathrm{EW_{FeK}} = 0.128$ keV, which yields a column

density $N_{\rm H} \approx 5 \times 10^{22}$ cm^{-2}. This value is in complete agreement with that derived by Corcoran et al. (1998), and suggests that cool material in front of the hard X-ray source provides the absorption and thus the origin of the fluorescent line.

In order to compare the X-ray emission of η Carina with previously published results, we calculated the unabsorbed X-ray flux in the 2–10 keV band obtaining a value of about 1400×10^{-13}, in fair agreement with the following published values: 800×10^{-13} for the probable quiescent phase, using *ASCA* observations (Corcoran et al. 2000); 1270×10^{-13} from *BeppoSAX* (Viotti et al. 2002); and $\approx 700 \times 10^{-13}$, applying a two-component model fit to *Chandra* data (Corcoran et al. 2001). However, these studies also report variations in the X-ray spectrum of η Carina of about one order of magnitude, related to the presence of an hypothesized companion star.

5 X-RAY TIME VARIABILITY

The first variability study of the X-ray emission from O-type stars was reported by Snow, Cash & Grady (1981), who found some evidence of long-term variations, although their results should be considered with caution, taking into account the limited sensitivity of the detectors available at that time. X-ray variability has been detected in the O-type stars Zeta Ori (Berghöfer & Schmitt 1994) and Theta[1] Ori C (Gagne et al. 1997). However, no significant variability was detected by the *ROSAT* All-Sky Survey in the X-ray emission of 57 OB stars over a time-scale of ≈2 d (Berghöfer & Schmitt 1995).

We explored the possibility of short-term X-ray variability of the sources detected in the *XMM–Newton* data, first from revolution 115 (about 33 ks of data), and then from revolution 116 (about 10 ks). For each X-ray source, we extracted a light curve from the EPIC PN and EPIC MOS-1 data, using a circular region centred on the source. We also extracted, for each revolution data set, a background light curve from a source-free circular region close to the source. The extracted light curves for the brightest objects were rebinned adopting bins of 180 s for each analysed source, except for η Carina for which we adopted bins of 60 s. The X-ray variability was analysed through the estimation of the unweighted average count rates ($\overline{x}$) and their dispersion ($\sigma_{\rm x}$), which were used as parameters for a Student-T test. Then a statistical significance level for the observed variability was obtained (see Table 4). To eliminate any background fluctuation that could include a systematic error in the time analysis, we applied the same statistical test to X-ray sources supposed to be constant, finding no X-ray variability for them. However, the assumed normal statistical distribution adopted in the Student-T test can introduce uncertainties, although smaller than 10 per cent, because of the Poissonian distribution in the image.

In Table 4, we present the results of this temporal analysis for X-ray sources which display variability above a confidence level of 60 per cent for the time interval of about 50 h covered by the observations.

Table 4. X-ray time variability for several detected sources. $\overline{x}$ represents the unweighted average count rate, and $\sigma_{\rm x}$ the intrinsic light-curve dispersion. A † is used to indicate an X-ray flare.

Source	Rev. 115		Rev. 116		Prob.
	$\overline{x}$	$\sigma_{\rm x}$	$\overline{x}$	$\sigma_{\rm x}$	Var. (per cent)
15	0.015	0.007	0.03	0.01	66
26	0.015	0.009	0.035	0.014	78
28†	0.06	0.04	0.013	0.003	Flare-X
32	0.18	0.02	0.14	0.03	64
49	0.003	0.003	0.034	0.012	99
75	0.021	0.008	0.037	0.01	70

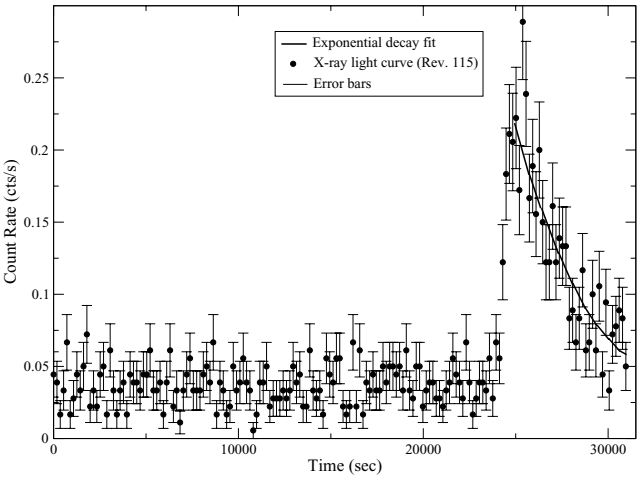

Figure 7. X-ray light curve observed for DETWC Tr 16 J104429.2−594143 (source 28). An intense flare is observed in the X-ray emission of this source (filled circles), which increases about six times in only 1.5 ks (≈40 min), followed by an exponential decrease (thick solid line) to reach the previous quiescent status. Error bars for each data point are also indicated.

In Fig. 7 we present data of an X-ray flare detected in DETWC Tr16 J104429.2-594143 (source 28), which lies only 11 arcsec south-west to the early B-type star Tr16-17 (Feinstein et al. 1973). This X-ray flare was detected near the end of the observation corresponding to revolution 115. At the beginning of the flare, the count rate increased by about a factor of 5 in only 40 min, and then it decreased exponentially to reach, about 1 h 30 min later, the initial quiescent level. The total time interval covered by this X-ray flare is about 2 h. A more detailed discussion of this event and the optical nature of this star will be provided in a forthcoming paper.

Another interesting feature was detected in the X-ray emission from source 49. No optical counterpart was identified for this source which presented a brightening of its X-ray emission along with an unstable fluctuation during revolution 116. The source increased its X-ray intensity by about three times compared to that observed in revolution 115 (36 h before). This behaviour is shown in Fig. 8. However, the position of the source over a CCD gap on the more sensitive EPIC PN camera, and its proximity to η Carina, could be affecting our data and any possible conclusions.

6 THE $L_{\rm x}$–$L_{\rm bol}$ RATIO

Several attempts have been made to identify the intrinsic properties responsible for the high dispersion observed in the $L_{\rm x}/L_{\rm bol}$ relation for OB-type stars. The usual expression $L_{\rm x}/L_{\rm bol} \sim 10^{-7}$ has been obtained from *Einstein* and *ROSAT* observations in the soft X-ray domain (0.2–2.4 keV). Regarding this relation, we bring to mind the useful discussion by Waldron et al. (1998) who point out the importance of distinguishing between the intrinsic and observed X-ray emission, and state that the canonical linear relation $L_{\rm x}/L_{\rm bol} \sim 10^{-7}$ stands only for ISM-corrected X-ray luminosities, shows a scatter of at least two orders of magnitude, and should be considered only as an observed property of OB stars.

Here we reconstruct the X-ray versus bolometric luminosity relation for several early-type stars placed within the Carina nebula, in the broad-band X-ray spectral region observed with *XMM–Newton* (0.3–12 keV).

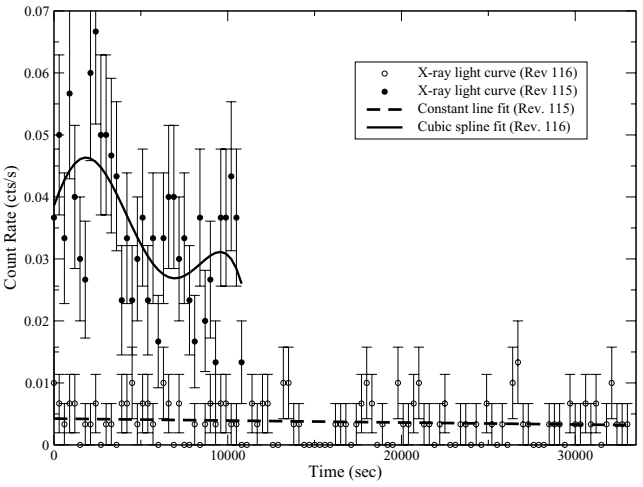

Figure 8. Superposition of X-ray light curves for the source 49 from observations of revolutions 115 and 116 (filled and open circles, respectively). The variability for the X-ray emission in revolution 116 is fitted by a cubic spline function (solid line). The observed behaviour of the X-ray emission in revolution 115 is well fitted by a constant function (thick dotted line). Error bars for each data point are also indicated.

The luminosities for the Carina nebula stars were calculated adopting the distance modulus of 11.76 ± 0.15 (2250 ± 180 pc), derived by Davidson et al. (2001) using *Hubble Space Telescope*/Space Telescope Imaging Spectrograph (*HST*/STIS) observations of the Homunculus nebula. The observed and corrected magnitudes were obtained from Massey & Johnson (1993) and the bolometric corrections from Chlebowski & Garmany (1991).

From Table 5 and Fig. 1, we see that several X-ray sources linked to early-type stars show an interesting diversity of soft, moderate and hard X-ray emission, suggesting a variety of physical phenomena acting on these stars. It is important now to address the question of how the inclusion of moderate and hard X-ray energies (above 2 keV) in the derivation of the X-ray luminosity function does affect the results of such derivation. From the O-type stars in the observed region, we choose those presenting an X-ray emission strong enough to allow the extraction of an X-ray spectrum and the determination of the X-ray luminosity from the adopted model. This sample includes several O-type stars, WR 25 and η Carina (see Table 6).

In Fig. 9 we construct the $L_{\rm x}$–$L_{\rm bol}$ luminosity relation for the 0.3–12 keV energy range with data from Table 6. A linear regression seems to be a good fit for most of the data points, except for three particular X-ray sources, η Carina, HDE 303311 and CPD-59° 2629, which show large excesses in their X-ray fluxes. This fact can be indicative of some physical X-ray mechanism affecting the intensity of the X-ray luminosity.

As seen in Fig. 9, the X-ray versus bolometric luminosity relation over the 0.3–12 keV energy range can be represented by a linear function in the log–log plane:

$$\mathrm{Log}(L_{\rm x}) = (-6.2 \pm 0.1) + (1.07 \pm 0.04)\mathrm{Log}(L_{\rm bol}).$$

This means that, in the $L_{\rm x}$–$L_{\rm bol}$ plane, this function becomes a constant relation: $L_{\rm x} \approx 6.0^{7.5}_{4.8} \times 10^{-7} L_{\rm bol}$.

This regression was obtained for the O-type stars in Table 6, excluding η Carina, WR 25, CPD-59° 2629 and HDE 303311. The slight difference with the canonical expression of 2×10^{-7}, formerly constructed from observations of early-type stars in the 0.3–2.4 keV energies, is mainly due to the adopted energy passband (0.3–12 keV), and probably not to an intrinsic difference in the $L_{\rm x}$–$L_{\rm bol}$ relation for the stars in this cluster (Corcoran et al. 1995). The similarity between both relations is not surprising, as soft X-ray emission below 2 keV produced by shock waves in the stellar wind dominates or at least strongly contaminates any emission at higher energies, except for intrinsically hard X-ray sources.

We also construct, for the same O-type stars, the $L_{\rm x}/L_{\rm bol}$ relation restricted to the 3–12 keV energy band, finding a strong deviation from the canonical $L_{\rm x}/L_{\rm bol}$ relation, as well as a very high dispersion of about four orders of magnitude, even excluding the two more deviant cases of η Carina and HDE 303311 (see Fig. 10). This indicates that the main mechanism responsible for the linear correlation found in the $L_{\rm x}/L_{\rm bol}$ relation for the 0.3–12 keV range is the emission at soft X-ray energies, which is probably produced through the radiatively driven stellar winds, and eventually in the colliding wind zones in binary systems.

In Fig. 10 we have also identified with different symbols those stars that are known to belong to binary or multiple systems and those for which no evidence of multiplicity has been reported. No clear correlation is found between the properties of the hard X-ray emission and the binary status of these stars, although the sample is too small to be statistically representative.

As can be seen in Fig. 9, there are large excesses in the unabsorbed X-ray fluxes obtained for the O5V star HDE 303311 (about 123×10^{-13} erg s^{-1} cm^{-2}) and for the O8.5 V star CPD-59° 2629 (Tr16-22). However, the derived unabsorbed luminosities are in general very dependent on the spectral model, which may have substantial systematic uncertainties. Also, uncertainties in the background subtraction can be an issue, especially considering the soft diffuse spatially varying X-ray emission associated with the Carina nebula. As a consequence, conclusions about the 'intrinsic' luminosities of these stars can be significantly biased.

In order to check the validity of these determinations, we performed some variations on the model for HDE 303311, using higher temperatures and lower absorption ($N_{\rm H}$) values. This resulted in fits of lower quality, with $\chi^2 \geqslant 2$ for 51 d.o.f., instead of $\chi^2 = 1.0$, obtained for the best fit (see Fig. 11). This means that the statistical significance of our best adopted fit is greater than 90 per cent with respect to the other tested models.

From Fig. 10 we see that HDE 303311 presents an intrinsic hard X-ray defect compared to other O-type stars in the region. Perhaps the high soft (<2 keV) luminosity observed for HDE 303311 is a consequence of the high density of the interstellar gas in the region where this star is located, which could be affected by the intense wind originating in this O5V star.

In the case of CPD-59° 2629 (Tr16-22) there seems to be an intrinsic X-ray overluminosity, because the estimated bolometric luminosity is in accordance with values usually adopted for O8.5 V stars (Schmidt-Kaler 1982). The exceptionally high X-ray flux from this star comes especially from energies above 2 keV (see Fig. 10), which is clearly noted in the fitted spectral model (see Table 3), and is also visible in Fig. 1. The binary status of this star is being explored in a current investigation.

A variety of different physical mechanisms can be responsible for the observed X-ray emission at soft and hard X-ray energies for these early-type stars. Those mechanisms are discussed in the next section.

7 DISCUSSION

The traditional view that hot massive stars emit only soft weakly absorbed X-rays (Lucy & White 1980; Lucy 1982) is now being replaced by a more complex picture that also requires emission from

Table 5. Count rate values for the detected sources over the whole observed energy range, and for each of the defined energy bands (soft, medium and hard) as measured on the MOS-1 and PN CCD images. The last column gives energy fluxes over the whole 0.3–12 keV observed energy range. A † refers to sources which lie over CCD gaps or outside the detection areas in one of the cameras; ‡ refers to extended or unresolved X-ray sources.

Source	MOS-1 [counts $s^{-1} \times 10^{-3}$]				PN [counts $s^{-1} \times 10^{-3}$]				Energy flux
	0.3–12 keV	Soft	Medium	Hard	0.3–12 keV	Soft	Medium	Hard	$\times 10^{-13}$ [cgs]
1†	6.1 ± 0.9	3 ± 0.8	2.5 ± 0.6	0.2 ± 0.4	–	–	–	–	0.8 ± 0.2
2	7 ± 1	3.9 ± 0.8	2.1 ± 0.5	0.2 ± 0.2	18 ± 2	8 ± 1	5 ± 1	1.1 ± 0.9	1.0 ± 0.2
3†	4.3 ± 0.7	2.3 ± 0.4	1.3 ± 0.3	0.2 ± 0.3	–	–	–	–	0.5 ± 0.2
4†	3.5 ± 0.9	1.9 ± 0.5	1.0 ± 0.3	0.1 ± 0.3	10 ± 1	4.4 ± 0.9	2.6 ± 0.6	0.8 ± 0.6	0.6 ± 0.1
5†	–	–	–	–	14 ± 2	10 ± 2	2.2 ± 0.4	1.1 ± 0.8	0.8 ± 0.2
6†	4.6 ± 0.9	2.4 ± 0.3	1.5 ± 0.4	0.3 ± 0.5	–	–	–	–	0.6 ± 0.1
7†	5.8 ± 0.9	2.6 ± 0.5	1.6 ± 0.3	0.1 ± 0.3	–	–	–	–	0.8 ± 0.2
8	6 ± 1	2.6 ± 0.7	1.6 ± 0.4	0.1 ± 0.3	–	–	–	–	0.8 ± 0.3
9	5 ± 1	2.8 ± 0.5	1.0 ± 0.3	0.3 ± 0.4	14 ± 2	8 ± 1	3.4 ± 0.6	0.3 ± 0.4	0.8 ± 0.2
10	5.7 ± 0.6	4.4 ± 0.9	0.7 ± 0.1	0.2 ± 0.3	13 ± 1	7 ± 1	1.7 ± 0.5	0.2 ± 0.3	0.5 ± 0.2
11‡	100 ± 5	72 ± 4	10 ± 1	5 ± 1	307 ± 10	226 ± 7	24 ± 3	15 ± 2	16 ± 5
12†	3.8 ± 0.6	3.6 ± 0.8	0.5 ± 0.4	0.2 ± 0.2	–	–	–	–	0.5 ± 0.1
13	4.2 ± 0.6	3.0 ± 0.5	1.0 ± 0.3	0.2 ± 0.2	21 ± 2	17 ± 2	2.5 ± 0.5	0.3 ± 0.2	0.9 ± 0.3
14	6 ± 1	3.4 ± 0.6	0.5 ± 0.4	0.2 ± 0.3	–	–	–	–	0.8 ± 0.2
15	–	–	–	–	9 ± 1	5 ± 1	2.0 ± 0.4	0.2 ± 0.3	0.4 ± 0.1
16‡	6 ± 1	5.0 ± 0.8	0.2 ± 0.3	0.2 ± 0.4	23 ± 2	20 ± 2	0.5 ± 0.4	0.2 ± 0.4	1.0 ± 0.2
17‡	14 ± 2	11 ± 1	2 ± 0.2	0.5 ± 0.4	45 ± 5	38 ± 3	5 ± 1	1 ± 0.3	4 ± 2
18	–	–	–	–	11 ± 1	9 ± 1	2.2 ± 0.7	0.9 ± 0.3	0.6 ± 0.2
19‡	339 ± 7	236 ± 5	65 ± 3	12 ± 1	1238 ± 10	903 ± 8	217 ± 6	52 ± 3	58 ± 13
20†	16 ± 2	7 ± 1	5.7 ± 0.9	2.5 ± 0.7	–	–	–	–	2.1 ± 0.4
21	7 ± 1	4 ± 0.4	3.0 ± 0.6	0.2 ± 0.3	11 ± 1	6 ± 0.3	4.9 ± 0.9	5 ± 1	0.8 ± 0.2
22†	3.5 ± 0.7	1.8 ± 0.3	1.2 ± 0.3	0.4 ± 0.2	–	–	–	–	0.5 ± 0.1
23	–	–	–	–	6 ± 1	3.9 ± 0.7	2.6 ± 0.5	0.4 ± 0.3	0.3 ± 0.1
24	4.2 ± 0.6	2.3 ± 0.5	1.3 ± 0.3	0.5 ± 0.1	13 ± 1	8 ± 1	3.5 ± 0.5	1.4 ± 0.3	0.6 ± 0.1
25	–	–	–	–	3.8 ± 0.6	3.3 ± 0.6	0.9 ± 0.4	0.5 ± 0.4	0.2 ± 0.1
26	2.2 ± 0.5	1.7 ± 0.4	0.2 ± 0.4	0.1 ± 0.5	7 ± 1	5.4 ± 0.1	0.4 ± 0.3	0.1 ± 0.3	0.4 ± 0.1
27	2.1 ± 0.5	1.4 ± 0.4	0.2 ± 0.4	0.1 ± 0.5	–	–	–	–	0.3 ± 0.1
28	7.2 ± 0.6	4.0 ± 0.5	2.1 ± 0.3	1.1 ± 0.3	26 ± 1	16 ± 1	6.5 ± 0.7	3.3 ± 0.5	1.2 ± 0.2
29	7.6 ± 0.6	6.4 ± 0.5	0.5 ± 0.4	0.1 ± 0.2	27 ± 2	17 ± 0.7	4.2 ± 0.3	0.2 ± 0.4	0.6 ± 0.1
30†	2.2 ± 0.5	1.3 ± 0.3	1.3 ± 0.4	0.2 ± 0.3	13 ± 1	7 ± 1	3.0 ± 0.5	0.4 ± 0.4	0.5 ± 0.2
31	–	–	–	–	19 ± 2	12 ± 1	2.4 ± 0.5	0.2 ± 0.3	1.1 ± 0.1
32	42 ± 2	38 ± 2	1.1 ± 0.3	0.3 ± 0.4	149 ± 5	143 ± 4	2.7 ± 0.6	0.2 ± 0.3	7.1 ± 1.5
33	4.0 ± 0.6	2.9 ± 0.7	0.4 ± 0.4	0.2 ± 0.3	12 ± 2	6 ± 1	2.1 ± 0.4	0.4 ± 0.4	0.6 ± 0.1
34†	–	–	–	–	12 ± 1	7 ± 1	3.4 ± 0.6	3.8 ± 0.6	0.7 ± 0.1
35	11 ± 1	7.2 ± 0.8	4 ± 0.3	0.5 ± 0.4	35 ± 2	22 ± 2	5 ± 0.4	4 ± 0.7	0.9 ± 0.2
36	4.1 ± 0.8	3.9 ± 0.7	0.3 ± 0.4	0.2 ± 0.4	34 ± 2	30 ± 1	2.4 ± 0.5	0.3 ± 0.4	1.9 ± 0.4
37‡	137 ± 3	104 ± 3	19 ± 1	4.3 ± 0.5	274 ± 6	218 ± 5	28 ± 2	8 ± 1	17 ± 1
38	5 ± 1	3.9 ± 0.7	1.4 ± 0.3	0.2 ± 0.3	11 ± 2	7 ± 1	0.2 ± 0.3	0.1 ± 0.3	0.6 ± 0.1
39	2.9 ± 0.6	1.7 ± 0.4	0.7 ± 0.4	0.2 ± 0.3	10 ± 2	7 ± 1	0.5 ± 0.4	0.2 ± 0.4	0.2 ± 0.1
40	3.0 ± 0.3	2.6 ± 0.4	0.4 ± 0.3	0.2 ± 0.3	15 ± 1	5.2 ± 0.5	7.3 ± 0.8	0.5 ± 0.4	0.6 ± 0.2
41	3.3 ± 0.5	3.4 ± 0.5	0.8 ± 0.4	0.2 ± 0.3	11 ± 1	12 ± 1	1.2 ± 0.3	0.6 ± 0.4	0.5 ± 0.1
42	2.0 ± 0.3	1.3 ± 0.3	0.4 ± 0.3	0.2 ± 0.2	5.0 ± 0.6	3.7 ± 0.5	0.6 ± 0.3	0.3 ± 0.3	0.2 ± 0.1
43	5.0 ± 0.6	2.6 ± 0.4	1.7 ± 0.3	0.3 ± 0.4	15 ± 1	8 ± 1	4.1 ± 0.6	2.0 ± 0.3	0.7 ± 0.1
44†	13 ± 2	5 ± 0.4	3.2 ± 0.8	0.3 ± 0.3	33 ± 3	8 ± 0.4	2.9 ± 0.31	1.0 ± 0.2	1.8 ± 0.1
45‡	39 ± 3	25 ± 2	3.7 ± 0.9	0.2 ± 0.3	–	–	–	–	5.2 ± 0.4
46†	6 ± 1	3.0 ± 0.2	2.4 ± 0.6	0.2 ± 0.4	–	–	–	–	0.8 ± 0.2
47	6.3 ± 0.8	5.5 ± 0.7	0.9 ± 0.2	0.2 ± 0.3	21 ± 2	19 ± 2	1.4 ± 0.3	0.3 ± 0.4	0.2 ± 0.2
48†	–	–	–	–	3.8 ± 0.6	2.7 ± 0.3	2.1 ± 0.4	0.5 ± 0.4	0.2 ± 0.1
49†	6.9 ± 0.9	3.8 ± 0.5	2.6 ± 0.4	0.2 ± 0.4	–	–	–	–	0.9 ± 0.1
50‡	1150 ± 8	132 ± 3	644 ± 6	374 ± 6	3350 ± 19	248.9 ± 6.1	1637 ± 13	1441 ± 12	173 ± 19
51†	16 ± 1	16 ± 1	1 ± 0.4	0.2 ± 0.4	14 ± 1	12 ± 1	3 ± 0.2	0.4 ± 0.3	2.2 ± 0.2
52	–	–	–	–	4.3 ± 0.8	3.9 ± 0.7	0.3 ± 0.3	0.1 ± 0.3	0.3 ± 0.1
53	–	–	–	–	6 ± 1	4.4 ± 0.8	1.0 ± 0.2	0.2 ± 0.3	0.3 ± 0.1
54	19 ± 1	13 ± 1	4.2 ± 0.8	0.9 ± 0.3	41 ± 2	29 ± 2	9 ± 1	1.5 ± 0.4	2.4 ± 0.1
55†	5.9 ± 0.9	3.1 ± 0.4	2.1 ± 0.5	1.5 ± 0.4	–	–	–	–	0.7 ± 0.2
56	2.9 ± 0.6	2.5 ± 0.5	0.2 ± 0.4	0.1 ± 0.4	11 ± 1	10 ± 1	0.5 ± 0.4	0.2 ± 0.4	0.4 ± 0.1
57	6 ± 1	2.7 ± 0.6	0.9 ± 0.2	0.2 ± 0.3	21 ± 2	20 ± 2	1.7 ± 0.3	0.5 ± 0.4	1.0 ± 0.2
58	4.4 ± 0.7	2.6 ± 0.5	0.3 ± 0.4	0.2 ± 0.3	6.5 ± 0.9	6.4 ± 0.9	0.5 ± 0.3	0.4 ± 0.4	0.5 ± 0.1
59	7 ± 1	6 ± 1	0.4 ± 0.3	0.2 ± 0.4	20 ± 1	20 ± 1	0.6 ± 0.3	0.2 ± 0.3	1.0 ± 0.1
60	–	–	–	–	3.0 ± 0.5	1.9 ± 0.3	0.5 ± 0.3	0.1 ± 0.3	0.2 ± 0.1
61	6 ± 1	2.5 ± 0.5	1.8 ± 0.3	7.9 ± 0.3	16 ± 1	8 ± 1	4.9 ± 0.5	1.8 ± 0.4	0.9 ± 0.1

Table 5 – *continued*

Source	MOS-1 [counts $s^{-1} \times 10^{-3}$]				PN [counts $s^{-1} \times 10^{-3}$]				Energy flux
	0.3–12 keV	Soft	Medium	Hard	0.3–12 keV	Soft	Medium	Hard	$\times 10^{-13}$ [cgs]
62	3.3 ± 0.6	2 ± 0.5	1.6 ± 0.3	0.1 ± 0.3	12 ± 1	4 ± 0.4	5.8 ± 0.8	3.4 ± 0.8	0.6 ± 0.2
63†	2.8 ± 0.6	2.2 ± 0.6	0.5 ± 0.2	0.2 ± 0.4	–	–	–	–	0.4 ± 0.1
64†	5.8 ± 0.3	5.6 ± 0.1	0.2 ± 0.2	0.1 ± 0.3	–	–	–	–	0.8 ± 0.1
65	4.9 ± 0.8	3.7 ± 0.7	0.4 ± 0.3	0.1 ± 0.3	19 ± 2	15 ± 1	0.9 ± 0.3	0.5 ± 0.4	0.8 ± 0.1
66	–	–	–	–	4.0 ± 0.6	3.0 ± 0.5	0.7 ± 0.4	0.2 ± 0.3	0.3 ± 0.1
67†	1.5 ± 0.3	1.1 ± 0.4	0.2 ± 0.6	0.1 ± 0.4	6.7 ± 0.8	5.8 ± 0.8	0.9 ± 0.3	0.2 ± 0.4	0.3 ± 0.1
68	3.3 ± 0.7	2.8 ± 0.6	0.2 ± 0.2	0.2 ± 0.3	7 ± 1	5 ± 1	0.5 ± 0.4	0.2 ± 0.3	0.4 ± 0.1
69	3.9 ± 0.7	2.2 ± 0.4	0.5 ± 0.3	0.2 ± 0.3	5 ± 1	3.2 ± 0.6	2.4 ± 0.5	0.5 ± 0.2	0.4 ± 0.1
70	–	–	–	–	8 ± 1	6.4 ± 0.3	2 ± 0.4	0.2 ± 0.2	0.4 ± 0.1
71	–	–	–	–	4.9 ± 0.4	3.2 ± 0.4	1.8 ± 0.5	0.9 ± 0.3	0.3 ± 0.1
72	7 ± 1	3.6 ± 0.7	3.4 ± 0.7	0.2 ± 0.3	15 ± 1	10 ± 1	2.9 ± 0.5	0.2 ± 0.3	0.9 ± 0.2
73	3.0 ± 0.6	1.9 ± 0.4	0.4 ± 0.4	0.2 ± 0.4	9 ± 1	7.7 ± 0.9	5.2 ± 0.4	0.6 ± 0.4	0.5 ± 0.1
74	–	–	–	–	8 ± 1	7 ± 1	0.9 ± 0.4	0.2 ± 0.4	0.5 ± 0.1
75	5 ± 1	3.7 ± 0.8	0.9 ± 0.3	0.2 ± 0.4	8 ± 1	6 ± 1	0.9 ± 0.4	0.3 ± 0.4	0.6 ± 0.2
76	2.4 ± 0.4	1.2 ± 0.2	1.1 ± 0.4	0.1 ± 0.3	7 ± 1	3.8 ± 0.6	1.2 ± 0.3	0.1 ± 0.3	0.4 ± 0.1
77†	6 ± 1	5 ± 1	0.6 ± 0.3	0.1 ± 0.3	10 ± 2	8 ± 1	0.7 ± 0.3	0.2 ± 0.3	0.7 ± 0.2
78†	10 ± 1	9 ± 1	0.8 ± 0.3	0.2 ± 0.3	27 ± 2	23 ± 2	3.2 ± 0.4	0.4 ± 0.3	1.4 ± 0.2
79	–	–	–	–	4 ± 1	3.9 ± 0.9	0.9 ± 0.2	0.2 ± 0.3	0.3 ± 0.1
80	–	–	–	–	6 ± 1	3.8 ± 0.7	2.2 ± 0.3	0.2 ± 0.3	0.4 ± 0.1

Table 6. The observed bolometric (L_{bol}) and X-ray (L_x) luminosities obtained for a distance of 2250 pc, expressed in cgs units.

Source name	Spectral type	L_{bol} [$\times 10^{38}$]	L_x[$\times 10^{32}$]		L_x/L_{bol}[$\times 10^{-7}$]	
			0.3–12 keV	3.0–12 keV	0.3–12 keV	3.0–12 keV
η Carina	LBV	200	$10\,868 \pm 1400$	670 ± 60	543 ± 60	33.5 ± 0.4
WR 25	WN6ha+O4f	72.5	186 ± 3	14.6 ± 0.4	25.6 ± 0.3	2.0 ± 0.1
HD 93205	O3V+O8V	22.0	23 ± 2	0.08 ± 0.002	10.4 ± 0.8	0.04 ± 0.01
HD 93250	O3((f))V	39.6	22 ± 2	3.5 ± 0.1	5.5 ± 0.1	0.9 ± 0.1
CPD-59 2629	O8.5V	3.1	20 ± 2	0.6 ± 0.1	64.5 ± 0.6	1.9 ± 0.1
HDE 303308	O3((f))	17.7	17 ± 2	0.95 ± 0.05	9.6 ± 0.1	0.54 ± 0.08
HD 93161	O6.5V	20.4	11 ± 1	0.05 ± 0.01	5.3 ± 0.5	0.025 ± 0.007
HD 93160	O6III(f)	15.1	4.0 ± 0.3	0.02 ± 0.009	2.6 ± 0.3	0.013 ± 0.006
HD 93204	O5V	8.8	6.7 ± 0.3	5.8×10^{-4}	7.6 ± 0.3	6.6×10^{-4}
FO 15	O4:5V	1.6	1.1 ± 0.1	0.38 ± 0.02	6.8 ± 0.3	2.4 ± 0.1
CPD-59 2636	O7V+O8V	5.8	2.5 ± 0.1	0.015 ± 0.008	4.3 ± 0.2	0.025 ± 0.009
CPD-59 2600	O5.5V	9.4	5.8 ± 0.4	7.3×10^{-4}	6.2 ± 0.1	7.8×10^{-4}
HDE 303311	O5V	6.0	74 ± 19	2.2×10^{-6}	123 ± 32	3.6×10^{-6}
CPD-59 2603	O7V+O9V	5.7	3.7 ± 0.3	3.1×10^{-4}	6.5 ± 0.1	5.6×10^{-4}
CPD-59 2641	O6V((f))	7.6	3.4 ± 0.5	4.5×10^{-4}	4.4 ± 0.1	6.0×10^{-4}

high-temperature plasma, originating close to the stars and through the wind.

Historically, the *instability driven wind shock* model has been the leading model to explain the soft X-ray emission, which is supposed to be distributed throughout the wind (Lucy & White 1980; Owocki, Castor & Ribicki 1988) from single hot stars. However, the broad-band (0.3–12 keV) observations here described present a new challenge for this model which predicts only soft weakly absorbed X-rays. Although this model has been able to explain the cool emission component on several massive hot stars (Lucy & White 1980), the hard emission component is not predicted by its current versions, and will thus require a different explanation. Moreover, if stellar X-rays suffered significant absorption by circumstellar material, in addition to wind absorption, then the radius at which the wind becomes optically thin (i.e. the X-ray emission radius) must be larger and hence the source would be intrinsically more luminous in X-rays (Owocki et al. 1988). If the wind is aspherical or inhomogeneous (presenting clumps, for example) then the expected X-ray luminosity for massive early-type stars could change significantly.

Magnetically confined wind shocks occur when the ionized wind is trapped by a dipolar magnetic field close to the base of the wind, and is then channelled along field lines toward the magnetic equatorial plane, where the two streams from the separate hemispheres collide to produce an X-ray emitting shock (Babel & Montmerle 1997). This process is able to produce high-temperature plasma, and can in principle explain the hard X-ray emission detected in some early-type stars. This model is favoured by the observation of rotational modulation in the X-ray and H_α emission of some O-type stars (Skinner et al. 2002). However, it seems quite difficult to justify this process in WR and LBV stars, which intrinsically have much larger mass-loss rates than O-type stars, and proportionally larger magnetic fields (of the order of several kG for WR stars) are required for wind confinement (Skinner et al. 2002).

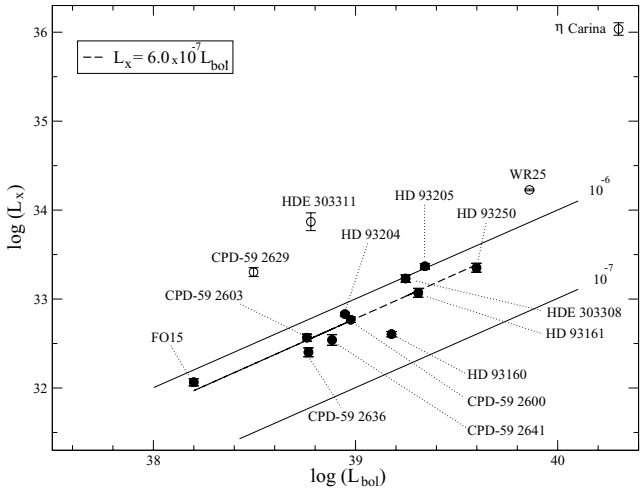

Figure 9. X-ray versus bolometric luminosity relation for several stars in the Carina nebula region in the broad-band 0.3–12 keV energies. The *X*-axis and *Y*-axis are plotted using a logarithmic scale. The open circles represent stars not considered in the linear regression.

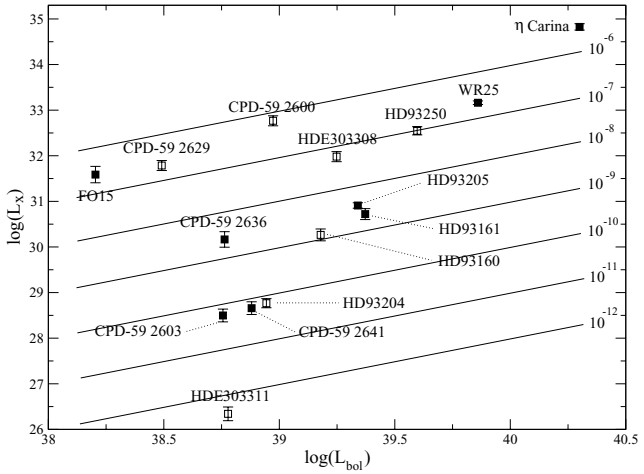

Figure 10. X-ray versus bolometric luminosity relation for O-type stars in the Carina nebula region in the hard broad-band 3–12 keV energies. Black symbols represent confirmed binary or multiple systems, and white symbols represent stars for which no evidence of multiplicity has been reported.

According to ud-Doula & Owocki (2002), the degree to which the wind is confined by the magnetic field is determined by the confinement parameter $\Gamma = {B_0}^2 {R_*}^2/\dot{M}v_\infty = 0.4{B_{100}}^2{R_{12}}^2/\dot{M}_{-6}v_8$, which characterizes the ratio between magnetic field energy density and kinetic energy density of the wind, where B_{100} is the surface equatorial field strength B_0 in 100 Gauss units, R_{12} in 10^{12} cm, $\dot{M}_{-6}$ in 10^{-6} $M_\odot$, and v_8 in 10^8 cm s^{-1}. ud-Doula & Owocki (2002) also found that, if $\Gamma \ll 1$, the field is fully opened by the wind outflow, but none the less for confinements as small as $\Gamma \approx 1/10$ it can have a significant back influence in enhancing the density and reducing the flow speed near the magnetic equator. Else, if $\Gamma \gg 1$, the wind is strongly confined and the magnetic field remains closed over a limited range of latitude, but eventually is opened into a nearly radial configuration. Within closed loops the flow is channelled toward loops into shock collisions that are strong enough to produce hard X-rays with the stagnated material then pulled by gravity back on to the star in quite complex and variable inflow. Now if we adopt

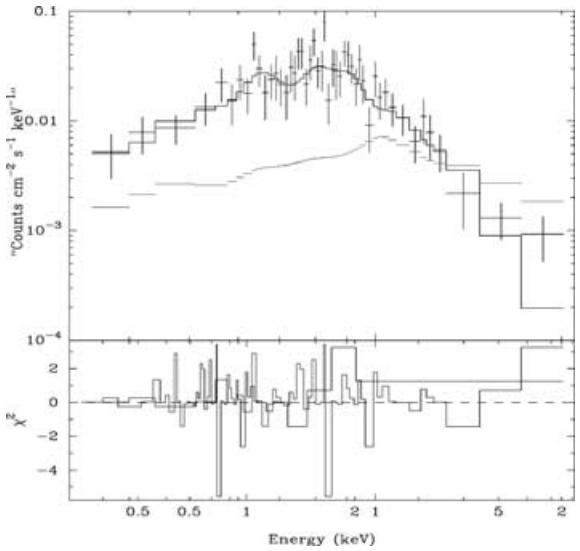

Figure 11. Upper panel: extracted EPIC PN spectrum of HDE 303311 rebinned to nine counts per channel. The adopted best fit (solid line) is compared with another model (broken line) of higher temperature (kT = 1.2 keV) and lower column density ($n_H = 0.2 \times 10^{22}$ cm^{-2}). Lower panel: χ^2 values for the best fit.

a typical magnetic field strength of about B_0 100 G ($B_{100} = 1$) for a late O-type star (Waldron & Cassinelli 2000), with typical radii of about 10 R $_\odot$ ($R_{12} = 0.69$), $\dot{M} \sim 10^{-7}$–10^{-6} ($\dot{M}_6 = 0.1-1$), and terminal velocities $v_\infty \approx$ 1000–3000 km s^{-1} (v_8 = 1–3), the magnetic confinement Γ is in the range 0.06–0.2. This means that most of the normal O-type stars have fully opened stellar winds. This scenario would then imply the presence of magnetic fields that are stronger than those measured for these types of stars, but also higher X-ray luminosities than derived via thermal emission plasma models applied to our *XMM–Newton* data.

For most of the binary and multiple systems identified as X-ray sources in our *XMM–Newton* image, the *colliding wind shocks* model seems the most straightforward explanation for the detected X-ray emission. Although the temperature of the hot component is not tightly constrained, spectral fits with optically thin plasma models are consistent with values as high as $kT_{hot} \approx 5$ keV (see Section 4). Such a high temperature could be produced in a wind collision zone for O+O and WR+O binary systems with strong stellar winds. The collision zone forms an adiabatic shock region near the surface of the component whose wind is the less strong (Usov 1992). Then we can safely assume the immediate post-shock density, velocity and temperature to be given by strong shock limits appropriate for $\gamma = 5/3$ (adiabatic index), $\rho_s \approx 4\rho_w$, $v_s = v_w/4$ and $kT_s = 3m{v_s}^2/16$. Then for $m \approx 10^{-24}$ g per particle (solar abundance), the temperature between the wind shocks is of the order of $1.4 \times 10^7 {v_8}^2$ K (=$1.2{v_8}^2$ keV), where v_8 is the pre-shock wind velocity in 10^8 cm s^{-1} (Stevens, Blondin & Pollock 1992). Now, assuming a typical pre-shock wind velocity range of about 1000–2000 km s^{-1} for late O to early B and WR stars, respectively (Stevens et al. 1992), we obtain a gas temperature range of $kT_s \approx 0.75$–5 keV, which agrees with the typical temperature obtained for several known O-type binary stars detected as X-ray sources. However, according to the different separations between binary components, inhibition (Stevens & Pollock 1994) and sudden radiative breaking acceleration (Gayley, Owicki & Cramer 1997) of the most intense of the winds may change significantly, affecting the strength of the

wind–wind collision, and thus the intensity of the X-ray emission (Owocki & Gayley 1995). These physical conditions acting in the collision zone of confirmed binaries can be detected through the analysis of phase-locked variations of the X-ray emission from these sources. Detectable orbital variability of the X-ray emission can be produced in different ways, e.g. varying separation between stars in eccentric orbits, anisotropic absorption and phase-dependent X-ray emission, asymmetry and inhomogeneities of the wind, photospheric eclipses in high inclination systems, etc. (Pittard & Stevens 1997). Eventually, we did not detect any variability in the X-ray flux of most of our well-known binary and multiple stars, as we would have expected from this model. However, we do not discard the possibility of detecting such variations, especially considering that our time baseline ($\approx$10 h) is shorter than the orbital periods of all of these systems.

Finally, the *non-thermal X-ray emission* model proposed by Chen & White (1991) explains the production of hard X-ray photons in hot stars by inverse Compton scattering of stellar ultraviolet photons off relativistic shock-accelerated particles in the wind. This model has relevance for all hot stars subject to line-driven instabilities. The X-rays generated from this mechanism are not expected to show large amplitude variations, and this is consistent with the temporal behaviour of most of the detected X-ray sources. However, bremsstrahlung X-ray emission may be as important as inverse Compton scattering in dense stellar winds (Chen & White 1991). As noted in Section 4, we cannot rule out a power-law model for some hard X-ray sources, based on X-ray spectral model fits. We therefore suggest that some of the unexpectedly hard X-ray sources detected could be massive pre-main-sequence stars with gas accretion events, which could generate violent jets mainly composed by relativistic electrons. Moreover, the inverse Compton effect is not expected to show large amplitude variations, which is consistent with the temporal behaviour of most of the OB-type stars analysed here.

8 SUMMARY

We have used *XMM–Newton* telescope observations of the Carina nebula (NGC 3372) to obtain a high-quality X-ray image of this region. Subsequent analysis of these data reveals a great number of faint point-like X-ray sources in addition to several bright early-type massive stars. We have shown that about 70 per cent of the detected X-ray sources have optical counterparts inside the Carina nebula, although we caution that some of the detected sources could be foreground (or background) objects that contaminate our sample.

Among the 80 X-ray sources detected on the combined EPIC PN and MOS-1 image, about 20 per cent were detected for the first time. Moreover, we obtained information about the energy distribution for each source, by splitting the observational data into three independent X-ray energy bands. This produced unexpected views of some of the detected sources, and raised new questions about the origin of the X-ray emission in massive hot stars, and their correlation with the bolometric luminosity. In the process of analysing the hardness of the detected sources and fitting models to the observed X-ray spectra, we obtained some clues on the different physical mechanisms that could be responsible for the X-ray emission from those stars.

Our general interpretation for most of the detected soft X-ray sources agrees with the typical X-ray properties of early-type stars, where the 0.3–2 keV X-ray emission could be originated in shocks within the radiation-driven stellar winds, and is related to the bolometric luminosity by the canonical expression $L_{\rm x}/L_{\rm bol}\sim 10^{-7}$. Moreover, most of the detected X-ray sources have soft X-ray spectra with typical temperatures kT between 0.1–0.5 keV, and luminosities of a few times 10^{31} erg s^{-1}.

We analyse separately the broad 0.3–12 keV and the hard 3.0–12 keV energy ranges for several O-type stars, the Wolf–Rayet star WR 25 and the LBV η Carina. The first relation agrees with the traditional relation between $L_{\rm x}$ and $L_{\rm bol}$, although with a larger value for the constant: $6.0^{7.5}_{4.8} \times 10^{-7}$, compared to the 'canonical' 2.0×10^{-7}. In contrast, the $L_{\rm x}/L_{\rm bol}$ ratio for hard energies shows a strong deviation from the canonical relation, as well as a very high dispersion. This suggests that for most of these stars the mechanisms responsible for the soft X-ray emission dominate over the physical processes producing hard X-rays. As for the hard emission, we were unable to find any trend with the spectral types or the binary status of the analysed stars, although our sample is too small to be statistically representative and more studies are needed in order to understand the observed hard X-ray properties of these sources.

Most of the detected X-ray sources do not seem to show any significant X-ray variability along the 48 hours of time baseline covered by these observations. However, some faint X-ray sources show an unusual intrinsic variability, which could be indicative of a pre-main-sequence phase, for example. Unfortunately, optical spectra of these sources are not available to the authors at the present time, and we cannot rule out the possibility of foreground low mass stars, whose X-rays originate from coronal activity.

Among the observed O-type stars with X-ray emission strong enough to analyse their X-ray spectrum, we found two peculiar sources which present unexpected X-ray excesses. We found an intrinsic hard X-ray overluminosity for CPD-59° 2629 (Tr16-22), corresponding to $L_{\rm x}/L_{\rm bol} \approx 6.45 \times 10^{-6}$, about one order of magnitude higher than expected for an O8.5 V star. Moreover, the spectral distribution of its X-ray emission agrees with a hot multitemperature model of about 0.4–2.5 keV (4.5×10^6–3×10^7 K), which can be easily observed in the colour X-ray image (Fig. 1). An optical investigation is at present being conducted in order to explore a possible multiple nature of this interesting star. The other star presenting X-ray overluminosity (this time in the soft X-ray domain) is HDE 303311. This star shows an intrinsic overabsorption value $N_{\rm H}$ of about 0.8×10^{22} cm^{-2} linked to an X-ray luminosity of 123×10^{32} erg s^{-1}, about two orders of magnitude above the value expected for an O5V star.

Another interesting fact needing confirmation is that the spectra of the brightest stars seem to be best fitted by low-metallicity models, varying between 0.2 and 0.7 times the solar abundance.

ACKNOWLEDGMENTS

This work is based on observations obtained with *XMM–Newton*, a European Space Agency (ESA) science mission with instruments and contributions directly funded by ESA member states and the US (NASA). We thank the whole *XMM–Newton* team for producing well-calibrated data, and especially Dr Carlos Gabriel, member of the *XMM–Newton* SOC at VILSPA, Spain, for helpful advice in the early analysis of these data. We thank R. Barbá, G. Bosch and V. Niemela for many very useful discussions and comments along the development of this work. We made use of the FTOOLS suite of software supported by the HEASARC. This research has made use of NASA's Astrophysics Data System Abstract Service. We are deeply indebted to our referee, Mike Corcoran, for many useful suggestions and a careful revision of our manuscript.

REFERENCES

Albacete Colombo J. F., Morrell N., Niemela V., Corcoran M., 2001, MNRAS, 326, 78

Albacete Colombo J. F., Morrell N., Rauw G., Corcoran M., Niemela V., Sana H., 2002, MNRAS, 336, 1099

Arnaud K. A., 1996, in Jacoby G., Barnes J., eds, ASP Conf. Ser. Vol. 101, Astronomical Data Analysis Software and Systems V. Astron. Soc. Pac., San Francisco, p. 17

Babel J., Montmerle T., 1997, A&A, 323, 121

Berghöfer T. W., Schmitt J. H. M. M., 1994, Sci, 265, 1689

Berghöfer T. W., Schmitt J. H. M. M., 1995, AdSpR, 16, 163

Cash W., 1979, ApJ, 228, 939

Chen W., White R. L., 1991, ApJ, 336, 512

Chlebowski T., Garmany C.D., 1991, AJ, 368, 241

Chlebowski T., Harnden F. R., Jr, Sciortino S., 1989, ApJ, 341, 427

Corcoran M., Rawley G. L., Swank H. J., Petre R., Schmitt J., Day C., 1995, RevMexAACS, 2, 97

Corcoran M. F. et al., 1998, ApJ, 494, 381

Corcoran M. F., Pittard J. M., Marchenko S. V., The XMEGA Group, 1999, in van der Hucht K. A., Koenigsberger G., Eenens P. R. J., eds, IAU Symp. 193, Wolf–Rayet Phenomena in Massive Stars and Starburst Galaxies. Astron. Soc. Pac., San Francisco, p. 772

Corcoran M. F., Fredericks A. C., Petre R., Swank J. H., Drake S. A., 2000, ApJ, 545, 420

Corcoran M. F. et al., 2001, AJ, 562, 1031

Cudworth K. M., Martin S. C., DeGioia-Eastwood K., 1993, AJ, 105, 1822

Davidson K., Smith N., Gull R. T., Ishibashi K., 2001, AJ, 121, 1569

DeGioia-Eastwood K., Throop H., Walker G., Cudworth K., 2001, 549, 578

Feinstein A., Marraco H. G., Muzzio J. C., 1973, A&AS, 12, 331

Feigelson E. D., Broos P., Gaffney J. A. III, Garmire G., Hillenbrand L. A., Pravdo S. H., Townsley L., Tsuboi Y., 2002, ApJ, 574, 258

Gagne M., Caillault J.-P., Stauffer J. R., Linsky J. L., 1997, ApJL, 478, 87

Gayley K. G., Owicki S. P., Cramer S. R., 1997, AJ, 475, 786

Jansen F. et al., 2001, A&A, 365, L1

Kallman T., 1995, ApJ, 455, 603

Lautenegger M. A., Kahn S. M., Ramsay G., 2003, ApJ, 585, 1015

Lucy L. B., 1982, ApJ, 255, 286

Lucy L. B., White R. L., 1980, ApJ, 241, 300

Maeda Y., Tsuboi Y., 1999, AAS, 31, 1541

Massey P., Johnson J., 1993, AJ, 105, 980

Micela G., Sciortino S., Damiani F., Maggio A., 1997, ApJ, 483, 350

Morrison R., McCammon D., 1983, ApJ, 270, 119

Morrell N. et al., 2001, MNRAS, 326, 85

Owocki S. P., Gayley K. G., 1995, AJ, 454, L145

Owocki S. P., Castor J. I., Ribicki G. B., 1988, ApJ, 335, 914

Pittard J. M., Stevens I., 1997, MNRAS, 292, 298

Rauw G., Sana H., Antokhin I. I., Morrell N. I., Niemela V. S., Albacete Colombo J. F., Gosset E., Vreux J.-M., 2001, MNRAS, 336, 1149

Raymond J. C., Smith B. W., 1977, ApJS, 35, 419

Schmidt-Kaler Th., 1982, in Shaifers K., Voigt H. H., eds, Landolt-Börnstein, New Series. Group VI, Vol. 2/b, p. 455

Seward F. D., Chlebowski T., 1982, ApJ, 256, 530

Seward F. D., Forman W. R., Giacconi R., Griffiths R. E., Harnden F. R., Jr, Jones C., Pye J. P., 1979, ApJ, 234, 55

Skinner S. L., Zhekov S. A., Güdel M., Schmutz W., 2002, AJ, 572, 477

Snow T. P., Cash W., Grady C. A., 1981, ApJ, 244, 19

Stevens I. R., Pollock A. M. T., 1994, MNRAS, 269, 226

Stevens I. R., Blondin J. M., Pollock A. M. T., 1992, 386, 265

Strüder L. et al., 2001, A&A, 365, L18

Tanaka S., Kitamoto S., Suzuki T., Torii K., Corcoran M., Waldron W., 1998, IAUS, 188, 224

Turner M. J. L. et al., 2001, A&A, 365, L27

ud-Doula A., Owocki S. P., 2002, ApJ, 576, 413

Usov V. V., 1992, AJ, 389, 635

van der Hucht K. A., 2001, NewAR, 45, 135

Vikhlinin A., Forman W., Jones C., 1997, ApJL, 474, 7

Vikhlinin A., Pierre M., Gastaud R., 2001, A&A, 370, 689

Viotti R. F. et al., 2002, A&A, 385, 874

Waldron W. L., Cassinelli J. P., 2000, AJ, 548, L45

Waldron W. L., Corcoran M., Drake S. A., Smale A. P., 1998, ApJS, 118, 217

Wessolowski U., 1996, MPE Report, 236, 75

Zinnecker H., Preibisch T., 1994, A&A, 292, 152

This paper has been typeset from a TEX/LATEX file prepared by the author.